EUROPEAN ORGANISATION FOR NUCLEAR RESEARCH (CERN)

CERN-PH-EP-2014-168
LHCb-PAPER-2014-038
July 23, 2014

Measurement of *CP* asymmetry in $B_s^0 \to D_s^{\mp} K^{\pm}$ decays

The LHCb collaboration[†]

Abstract

We report on measurements of the time-dependent *CP* violating observables in $B_s^0 \to D_s^{\mp} K^{\pm}$ decays using a dataset corresponding to 1.0 fb^{-1} of pp collisions recorded with the LHCb detector. We find the *CP* violating observables $C_f = 0.53 \pm 0.25 \pm 0.04$, $A_f^{\Delta\Gamma} = 0.37 \pm 0.42 \pm 0.20$, $A_{\overline{f}}^{\Delta\Gamma} = 0.20 \pm 0.41 \pm 0.20$, $S_f = -1.09 \pm 0.33 \pm 0.08$, $S_{\overline{f}} = -0.36 \pm 0.34 \pm 0.08$, where the uncertainties are statistical and systematic, respectively. Using these observables together with a recent measurement of the B_s^0 mixing phase $-2\beta_s$ leads to the first extraction of the CKM angle γ from $B_s^0 \to D_s^{\mp} K^{\pm}$ decays, finding $\gamma = (115^{+28}_{-43})^{\circ}$ modulo 180° at 68% CL, where the error contains both statistical and systematic uncertainties.

Published in JHEP 11 (2014) 060

[†]Authors are listed at the end of this article.

1 Introduction

Time-dependent analyses of tree-level $B^0_{(s)} \to D^{\mp}_{(s)}\pi^{\pm}, K^{\pm}$ decays[1] are sensitive to the angle $\gamma \equiv \arg(-V_{ud}V^*_{ub}/V_{cd}V^*_{cb})$ of the unitarity triangle of the Cabibbo-Kobayashi-Maskawa (CKM) matrix [1, 2] through *CP* violation in the interference of mixing and decay amplitudes [3–5]. The determination of γ from such tree-level decays is important because it is not sensitive to potential effects from most models of physics beyond the Standard Model (BSM). The value of γ hence provides a reference against which other BSM-sensitive measurements can be compared.

Due to the interference between mixing and decay amplitudes, the physical *CP* violating observables in these decays are functions of a combination of γ and the relevant mixing phase, namely $\gamma + 2\beta$ ($\beta \equiv \arg(-V_{cd}V^*_{cb}/V_{td}V^*_{tb})$) in the B^0 and $\gamma - 2\beta_s$ ($\beta_s \equiv \arg(-V_{ts}V^*_{tb}/V_{cs}V^*_{cb})$) in the B^0_s system. A measurement of these physical observables can therefore be interpreted in terms of γ or $\beta_{(s)}$ by using an independent measurement of the other parameter as input.

Such measurements have been performed by both the BaBar [6, 7] and the Belle [8, 9] collaborations using $B^0 \to D^{(*)\mp}\pi^{\pm}$ decays. In these decays, however, the ratios $r_{D^{(*)}\pi} = |A(B^0 \to D^{(*)-}\pi^+)/A(B^0 \to D^{(*)+}\pi^-)|$ between the interfering $b \to u$ and $b \to c$ amplitudes are small, $r_{D^{(*)}\pi} \approx 0.02$, limiting the sensitivity on γ [10].

The leading order Feynman diagrams contributing to the interference of decay and mixing in $B^0_s \to D^{\mp}_s K^{\pm}$ are shown in Fig. 1. In contrast to $B^0 \to D^{(*)\mp}\pi^{\pm}$ decays, here both the $B^0_s \to D^-_s K^+$ ($b \to cs\bar{u}$) and $B^0_s \to D^+_s K^-$ ($b \to u\bar{c}s$) amplitudes are of the same order in the sine of the Cabibbo angle $\lambda = 0.2252 \pm 0.0007$ [11, 12], $\mathcal{O}(\lambda^3)$, and the amplitude ratio of the interfering diagrams is approximately $|V_{ub}V_{cs}/V_{cb}V_{us}| \approx 0.4$. Moreover, the decay width difference in the B^0_s system, $\Delta\Gamma_s$, is nonzero [13], which allows a determination of $\gamma - 2\beta_s$ from the sinusoidal and hyperbolic terms in the decay time evolution, up to a two-fold ambiguity.

This paper presents the first measurements of the *CP* violating observables in $B^0_s \to D^{\mp}_s K^{\pm}$ decays using a dataset corresponding to 1.0 fb^{-1} of pp collisions recorded with the LHCb detector at $\sqrt{s} = 7\,\text{TeV}$, and the first determination of $\gamma - 2\beta_s$ in these decays.

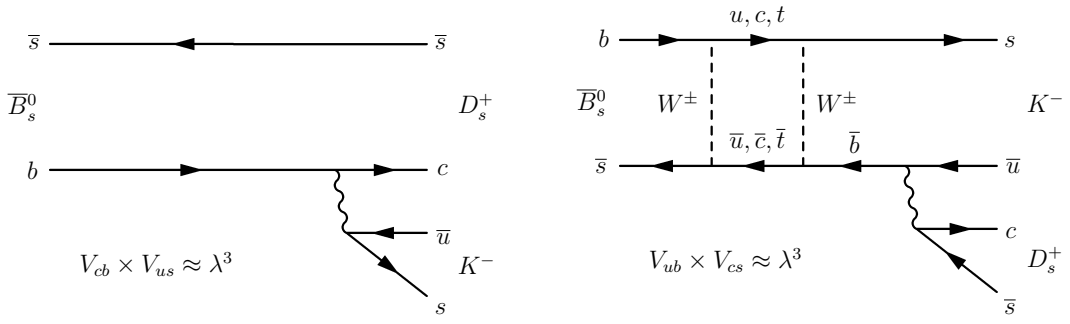

Figure 1: Feynman diagrams for $\overline{B}^0_s \to D^+_s K^-$ without (left) and with (right) B^0_s mixing.

[1] Inclusion of charge conjugate modes is implied except where explicitly stated.

1.1 Decay rate equations and CP violation observables

The time-dependent decay rates of the initially produced flavour eigenstates $|B_s^0(t=0)\rangle$ and $|\overline{B}_s^0(t=0)\rangle$ are given by

$$\frac{\mathrm{d}\Gamma_{B_s^0\to f}(t)}{\mathrm{d}t} = \frac{1}{2}|A_f|^2(1+|\lambda_f|^2)e^{-\Gamma_s t}\left[\cosh\left(\frac{\Delta\Gamma_s t}{2}\right) + A_f^{\Delta\Gamma}\sinh\left(\frac{\Delta\Gamma_s t}{2}\right) + C_f\cos\left(\Delta m_s t\right) - S_f\sin\left(\Delta m_s t\right)\right], \tag{1}$$

$$\frac{\mathrm{d}\Gamma_{\overline{B}_s^0\to f}(t)}{\mathrm{d}t} = \frac{1}{2}|A_f|^2\left|\frac{p}{q}\right|^2(1+|\lambda_f|^2)e^{-\Gamma_s t}\left[\cosh\left(\frac{\Delta\Gamma_s t}{2}\right) + A_f^{\Delta\Gamma}\sinh\left(\frac{\Delta\Gamma_s t}{2}\right) - C_f\cos\left(\Delta m_s t\right) + S_f\sin\left(\Delta m_s t\right)\right], \tag{2}$$

where $\lambda_f \equiv (q/p)(\overline{A}_f/A_f)$ and A_f ($\overline{A}_f$) is the decay amplitude of a B_s^0 to decay to a final state f ($\overline{f}$). Γ_s is the average B_s^0 decay width, and $\Delta\Gamma_s$ is the positive [14] decay-width difference between the heavy and light mass eigenstates in the B_s^0 system. The complex coefficients p and q relate the B_s^0 meson mass eigenstates, $|B_{L,H}\rangle$, to the flavour eigenstates, $|B_s^0\rangle$ and $|\overline{B}_s^0\rangle$

$$|B_L\rangle = p|B_s^0\rangle + q|\overline{B}_s^0\rangle\,, \tag{3}$$

$$|B_H\rangle = p|B_s^0\rangle - q|\overline{B}_s^0\rangle\,, \tag{4}$$

with $|p|^2+|q|^2=1$. Similar equations can be written for the CP-conjugate decays replacing C_f by $C_{\overline{f}}$, S_f by $S_{\overline{f}}$, and $A_f^{\Delta\Gamma}$ by $A_{\overline{f}}^{\Delta\Gamma}$. In our convention f is the $D_s^-K^+$ final state and $\overline{f}$ is $D_s^+K^-$. The CP asymmetry observables C_f, S_f, $A_f^{\Delta\Gamma}$, $C_{\overline{f}}$, $S_{\overline{f}}$ and $A_{\overline{f}}^{\Delta\Gamma}$ are given by

$$\begin{aligned} C_f &= \frac{1-|\lambda_f|^2}{1+|\lambda_f|^2} = -C_{\overline{f}} = -\frac{1-|\lambda_{\overline{f}}|^2}{1+|\lambda_{\overline{f}}|^2}\,,\\ S_f &= \frac{2\mathcal{I}m(\lambda_f)}{1+|\lambda_f|^2}\,, \quad A_f^{\Delta\Gamma} = \frac{-2\mathcal{R}e(\lambda_f)}{1+|\lambda_f|^2}\,,\\ S_{\overline{f}} &= \frac{2\mathcal{I}m(\lambda_{\overline{f}})}{1+|\lambda_{\overline{f}}|^2}\,, \quad A_{\overline{f}}^{\Delta\Gamma} = \frac{-2\mathcal{R}e(\lambda_{\overline{f}})}{1+|\lambda_{\overline{f}}|^2}\,. \end{aligned} \tag{5}$$

The equality $C_f = -C_{\overline{f}}$ results from $|q/p|=1$ and $|\lambda_f| = |\frac{1}{\lambda_{\overline{f}}}|$, *i.e.* the assumption of no CP violation in either the decay or mixing amplitudes. The CP observables are related to the magnitude of the amplitude ratio $r_{D_sK} \equiv |\lambda_{D_sK}| = |A(\overline{B}_s^0\to D_s^-K^+)/A(B_s^0\to D_s^-K^+)|$, the strong phase difference δ, and the weak phase difference $\gamma - 2\beta_s$ by the following

equations:

$$
\begin{aligned}
C_f =& \frac{1 - r_{D_sK}^2}{1 + r_{D_sK}^2}\,, \\
A_f^{\Delta\Gamma} = \frac{-2r_{D_sK}\cos(\delta - (\gamma - 2\beta_s))}{1 + r_{D_sK}^2}\,, &\quad A_{\overline{f}}^{\Delta\Gamma} = \frac{-2r_{D_sK}\cos(\delta + (\gamma - 2\beta_s))}{1 + r_{D_sK}^2}\,, \\
S_f = \frac{2r_{D_sK}\sin(\delta - (\gamma - 2\beta_s))}{1 + r_{D_sK}^2}\,, &\quad S_{\overline{f}} = \frac{-2r_{D_sK}\sin(\delta + (\gamma - 2\beta_s))}{1 + r_{D_sK}^2}\,.
\end{aligned} \tag{6}
$$

1.2 Analysis strategy

To measure the *CP* violating observables defined in Sec. 1.1, it is necessary to perform a fit to the decay-time distribution of the selected $B_s^0 \to D_s^{\mp}K^{\pm}$ candidates. The kinematically similar mode $B_s^0 \to D_s^-\pi^+$ is used as control channel which helps in the determination of the time-dependent efficiency and flavour tagging performance. Before a fit to the decay time can be performed, it is necessary to distinguish the signal and background candidates in the selected sample. This analysis uses three variables to maximise sensitivity when discriminating between signal and background: the B_s^0 mass; the D_s^- mass; and the log-likelihood difference $L(K/\pi)$ between the pion and kaon hypotheses for the companion particle.

In Sec. 4, the signal and background shapes needed for the analysis are obtained in each of the variables. Section 5 describes how a simultaneous extended maximum likelihood fit (in the following referred to as multivariate fit) to these three variables is used to determine the yields of signal and background components in the samples of $B_s^0 \to D_s^-\pi^+$ and $B_s^0 \to D_s^{\mp}K^{\pm}$ candidates. Section 6 describes how to obtain the flavour at production of the $B_s^0 \to D_s^{\mp}K^{\pm}$ candidates using a combination of flavour-tagging algorithms, whose performance is calibrated with data using flavour-specific control modes. The decay-time resolution and acceptance are determined using a mixture of data control modes and simulated signal events, described in Sec. 7.

Finally, Sec. 8 describes two approaches to fit the decay-time distribution of the $B_s^0 \to D_s^{\mp}K^{\pm}$ candidates which extract the *CP* violating observables. The first fit, henceforth referred to as the *sFit*, uses the results of the multivariate fit to obtain the so-called *sWeights* [15] which allow the background components to be statistically subtracted [16]. The *sFit* to the decay-time distribution is therefore performed using only the probability density function (PDF) of the signal component. The second fit, henceforth referred to as the *cFit*, uses the various shapes and yields of the multivariate fit result for the different signal and background components. The *cFit* subsequently performs a six-dimensional maximum likelihood fit to these variables, the decay-time distribution and uncertainty, and the probability that the initial B_s^0 flavour is correctly determined, in which all contributing signal and background components are described with their appropriate PDFs. In Sec. 10, we extract the CKM angle γ using the result of one of the two approaches.

2 Detector and software

The LHCb detector [17] is a single-arm forward spectrometer covering the pseudorapidity range $2 < \eta < 5$, designed for the study of particles containing b or c quarks. The detector includes a high-precision tracking system consisting of a silicon-strip vertex detector surrounding the pp interaction region [18], a large-area silicon-strip detector located upstream of a dipole magnet with a bending power of about 4 Tm, and three stations of silicon-strip detectors and straw drift tubes [19] placed downstream of the magnet. The tracking system provides a measurement of momentum, p, with a relative uncertainty that varies from 0.4% at low momentum to 0.6% at 100 GeV/c. The minimum distance of a track to a primary pp collision vertex, the impact parameter, is measured with a resolution of $(15 + 29/p_{\rm T})$ μm, where $p_{\rm T}$ is the component of p transverse to the beam, in GeV/c. Different types of charged hadrons are distinguished using information from two ring-imaging Cherenkov detectors [20]. The magnet polarity is reversed regularly to control systematic effects.

The trigger [21] consists of a hardware stage, based on information from the calorimeter and muon systems, followed by a software stage, which applies a full event reconstruction. The software trigger requires a two-, three- or four-track secondary vertex with a large sum of the transverse momentum of the charged particles and a significant displacement from the primary pp interaction vertices (PVs). A multivariate algorithm [22] is used for the identification of secondary vertices consistent with the decay of a b hadron.

In the simulation, pp collisions are generated using Pythia [23] with a specific LHCb configuration [24]. Decays of hadrons are described by EvtGen [25], in which final state radiation is generated using Photos [26]. The interaction of the generated particles with the detector and its response are implemented using the Geant4 toolkit [27, 28] as described in Ref. [29].

3 Event selection

The event selection begins by building $D_s^- \to K^-K^+\pi^-$, $D_s^- \to K^-\pi^+\pi^-$, and $D_s^- \to \pi^-\pi^+\pi^-$ candidates from reconstructed charged particles. These D_s^- candidates are subsequently combined with a fourth particle, referred to as the "companion", to form $B_s^0 \to D_s^\mp K^\pm$ and $B_s^0 \to D_s^- \pi^+$ candidates. The flavour-specific Cabibbo-favoured decay mode $B_s^0 \to D_s^- \pi^+$ is used as a control channel in the analysis, and is selected identically to $B_s^0 \to D_s^\mp K^\pm$ except for the PID criteria on the companion particle. The decay-time and B_s^0 mass resolutions are improved by performing a kinematic fit [30] in which the B_s^0 candidate is constrained to originate from its associated proton-proton interaction, *i.e.* the one with the smallest IP with respect to the B_s^0 candidate, and the B_s^0 mass is computed with a constraint on the D_s^- mass.

The $B_s^0 \to D_s^- \pi^+$ mode is used for the optimisation of the selection and for studying and constraining physics backgrounds to the $B_s^0 \to D_s^\mp K^\pm$ decay. The $B_s^0 \to D_s^\mp K^\pm$ and $B_s^0 \to D_s^- \pi^+$ candidates are required to be matched to the secondary vertex candidates found in the software trigger. Subsequently, a preselection is applied to the $B_s^0 \to D_s^\mp K^\pm$

and $B_s^0 \to D_s^- \pi^+$ candidates using a similar multivariate displaced vertex algorithm to the trigger selection, but with offline-quality reconstruction.

A selection using the gradient boosted decision tree (BDTG) [31] implementation in the TMVA software package [32] further suppresses combinatorial backgrounds. The BDTG is trained on data using the $B_s^0 \to D_s^- \pi^+$, $D_s^- \to K^- K^+ \pi^-$ decay sample, which is purified with respect to the previous preselection exploiting PID information from the Cherenkov detectors. Since all channels in this analysis are kinematically similar, and since no PID information is used as input to the BDTG, the resulting BDTG performs equally well on the other D_s^- decay modes. The optimal working point is chosen to maximise the expected sensitivity to the *CP* violating observables in $B_s^0 \to D_s^\mp K^\pm$ decays. In addition, the B_s^0 and D_s^- candidates are required to be within $m(B_s^0) \in [5300, 5800]\,\mathrm{MeV}/c^2$ and $m(D_s^-) \in [1930, 2015]\,\mathrm{MeV}/c^2$, respectively.

Finally, the different final states are distinguished by using PID information. This selection also strongly suppresses cross-feed and peaking backgrounds from other misidentified decays of b-hadrons to c-hadrons. We will refer to such backgrounds as "fully reconstructed" if no particles are missed in the reconstruction, and "partially reconstructed" otherwise. The decay modes $B^0 \to D^- \pi^+$, $B^0 \to D_s^- \pi^+$, $\overline{\Lambda}_b^0 \to \overline{\Lambda}_c^- \pi^+$, $B_s^0 \to D_s^\mp K^\pm$, and $B_s^0 \to D_s^{*-} \pi^+$ are backgrounds to $B_s^0 \to D_s^- \pi^+$, while $B_s^0 \to D_s^- \pi^+$, $B_s^0 \to D_s^{*-} \pi^+$, $B_s^0 \to D_s^- \rho^+$, $B^0 \to D_s^- K^+$, $B^0 \to D^- K^+$, $B^0 \to D^- \pi^+$, $\overline{\Lambda}_b^0 \to \overline{\Lambda}_c^- K^+$, $\overline{\Lambda}_b^0 \to \overline{\Lambda}_c^- \pi^+$, and $\Lambda_b^0 \to D_s^{(*)-} p$ are backgrounds to $B_s^0 \to D_s^\mp K^\pm$. This part of the selection is necessarily different for each D_s^- decay mode, as described below.

- For $D_s^- \to \pi^- \pi^+ \pi^-$ none of the possible misidentified backgrounds fall inside the D_s^- mass window. Loose PID requirements are nevertheless used to identify the D_s^- decay products as pions in order to suppress combinatorial background.

- For $D_s^- \to K^- \pi^+ \pi^-$, the relevant peaking backgrounds are $\overline{\Lambda}_c^- \to \overline{p} \pi^+ \pi^-$ in which the antiproton is misidentified, and $D^- \to K^+ \pi^- \pi^-$ in which both the kaon and a pion are misidentified. As this is the smallest branching fraction D_s^- decay mode used, and hence that most affected by background, all D_s^- decay products are required to pass tight PID requirements.

- The $D_s^- \to K^- K^+ \pi^-$ mode is split into three submodes. We distinguish between the resonant $D_s^- \to \phi \pi^-$ and $D_s^- \to K^{*0} K^-$ decays, and the remaining decays. Candidates in which the $K^+ K^-$ pair falls within $20\,\mathrm{MeV}/c^2$ of the ϕ mass are identified as a $D_s^- \to \phi \pi^-$ decay. This requirement suppresses most of the cross-feed and combinatorial background, and only loose PID requirements are needed. Candidates within a $50\,\mathrm{MeV}/c^2$ window around the K^{*0} mass are identified as a $D_s^- \to K^{*0} K^-$ decay; it is kinematically impossible for a candidate to satisfy both this and the ϕ requirement. In this case there is non-negligible background from misidentified $D^- \to K^+ \pi^- \pi^-$ and $\overline{\Lambda}_c^- \to \overline{p} \pi^- K^+$ decays which are suppressed through tight PID requirements on the D_s^- kaon with the same charge as the D_s^- pion. The remaining candidates, referred to as nonresonant decays, are subject to tight PID requirements on all decay products to suppress cross-feed backgrounds.

Figure 2 shows the relevant mass distributions for candidates passing and failing this PID selection. Finally a loose PID requirement is made on the companion track. After all selection requirements, fewer than 2% of retained events contain more than one signal candidate. All candidates are used in the subsequent analysis.

4 Signal and background shapes

The signal and background shapes are obtained using a mixture of data-driven approaches and simulation. The simulated events need to be corrected for kinematic differences between simulation and data, as well as for the kinematics-dependent efficiency of the PID selection requirements. In order to obtain kinematic distributions in data for this weighting, we use the decay mode $B^0 \to D^-\pi^+$, which can be selected with very high purity without the use of any PID requirements and is kinematically very similar to the

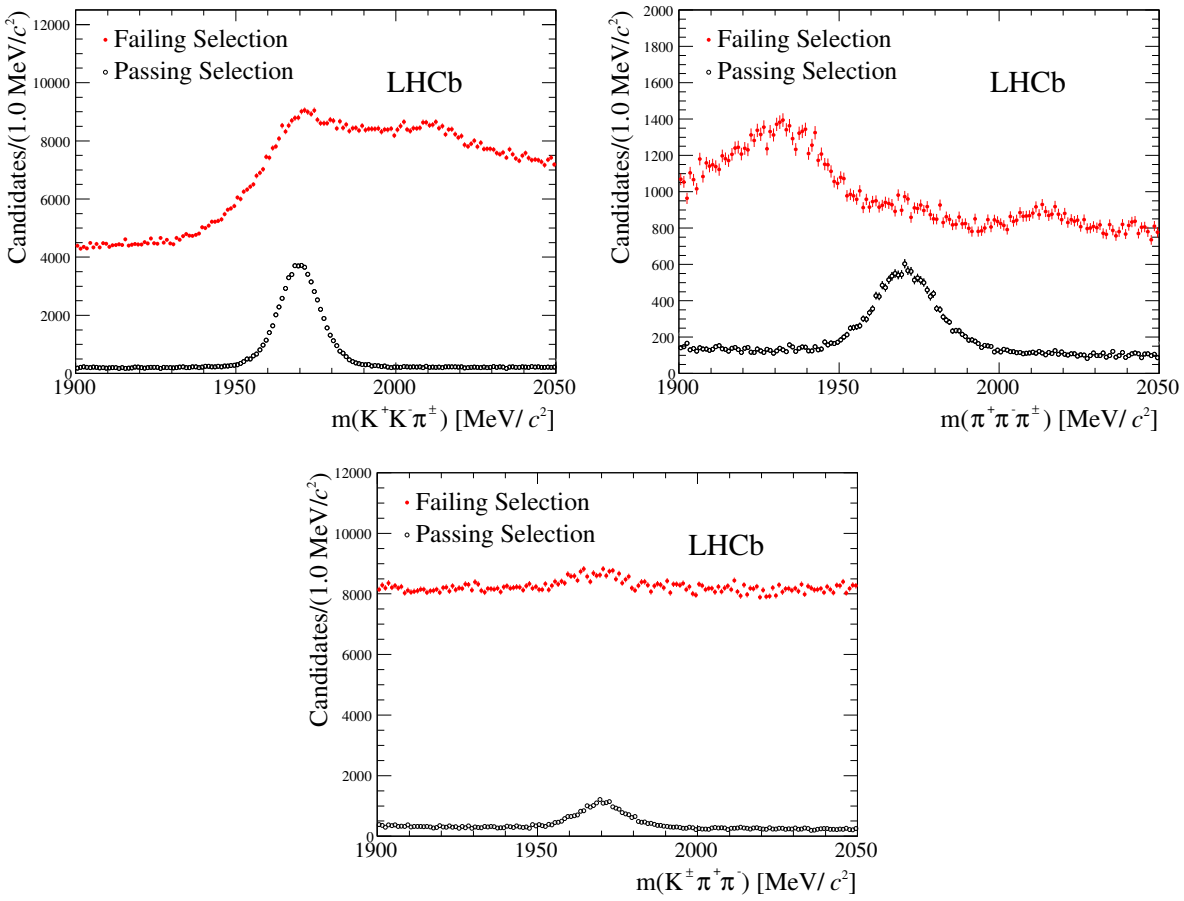

Figure 2: Mass distributions for D_s^- candidates passing (black, open circles) and failing (red, crosses) the PID selection criteria. In reading order: $D_s^- \to K^-K^+\pi^-$, $D_s^- \to \pi^-\pi^+\pi^-$, and $D_s^- \to K^-\pi^+\pi^-$.

B_s^0 signals. The PID efficiencies are measured as a function of particle momentum and event occupancy using prompt $D^{*+} \to D^0(K^-\pi^+)\pi^+$ decays which provide pure samples of pions and kaons [33], henceforth called D^{*+} calibration sample.

4.1 $\mathbf{B_s^0}$ candidate mass shapes

In order to model radiative and reconstruction effects, the signal shape in the B_s^0 mass is the sum of two Crystal Ball [34] functions with common mean and oppositely oriented tails. The signal shapes are determined separately for $B_s^0 \to D_s^{\mp} K^{\pm}$ and $B_s^0 \to D_s^- \pi^+$ from simulated candidates. The shapes are subsequently fixed in the multivariate fit except for the common mean of the Crystal Ball functions which floats for both the $B_s^0 \to D_s^- \pi^+$ and $B_s^0 \to D_s^{\mp} K^{\pm}$ channel.

The functional form of the combinatorial background is taken from the upper B_s^0 sideband, with its parameters left free to vary in the subsequent multivariate fit. Each D_s^- mode is considered independently and parameterised by either an exponential function or by a combination of an exponential and a constant function.

The shapes of the fully or partially reconstructed backgrounds are fixed from simulated events using a non-parametric kernel estimation method (KEYS, [35]). Exceptions to this are the $B^0 \to D^- \pi^+$ background in the $B_s^0 \to D_s^- \pi^+$ fit and the $B_s^0 \to D_s^- \pi^+$ background in the $B_s^0 \to D_s^{\mp} K^{\pm}$ fit, which are obtained from data. The latter two backgrounds are reconstructed with the "wrong" mass hypothesis but without PID requirements, which would suppress them. The resulting shapes are then weighted to account for the effect of the momentum-dependent efficiency of the PID requirements from the D^{*+} calibration samples, and KEYS templates are extracted for use in the multivariate fit.

4.2 $\mathbf{D_s^-}$ candidate mass shapes

The signal shape in the D_s^- mass is again a sum of two Crystal Ball functions with common mean and oppositely oriented tails. The signal shapes are extracted separately for each D_s^- decay mode from simulated events that have the full selection chain applied to them. The shapes are subsequently fixed in the multivariate fit except for the common mean of the Crystal Ball functions, which floats independently for each D_s^- decay mode.

The combinatorial background consists of both random combinations of tracks which do not peak in the D_s^- mass, and, in some D_s^- decay modes, backgrounds that contain a true D_s^-, and a random companion track. It is parameterised separately for each D_s^- decay mode either by an exponential function or by a combination of an exponential function and the signal D_s^- shape.

The fully and partially reconstructed backgrounds which contain a correctly reconstructed D_s^- candidate ($B_s^0 \to D_s^{\mp} K^{\pm}$ and $B^0 \to D_s^- \pi^+$ as backgrounds in the $B_s^0 \to D_s^- \pi^+$ fit; $B^0 \to D_s^- K^+$ and $B_s^0 \to D_s^- \pi^+$ as backgrounds in the $B_s^0 \to D_s^{\mp} K^{\pm}$ fit) are assumed to have the same mass distribution as the signal. For other backgrounds, the shapes are KEYS templates taken from simulated events, as in the B_s^0 mass.

4.3 Companion L(K/π) shapes

We obtain the PDFs describing the $L(K/\pi)$ distributions of pions and kaons from dedicated D^{*+} calibration samples. We obtain the PDF describing the protons using a calibration sample of $\Lambda_c^+ \to pK^-\pi^+$ decays. These samples are weighted to match the signal kinematic and event occupancy distributions in the same way as the simulated events. The weighting is done separately for each signal and background component, as well as for each magnet polarity. The shapes for each magnet polarity are subsequently combined according to the integrated luminosity in each sample.

The signal companion $L(K/\pi)$ shape is obtained separately for each D_s^- decay mode to account for small kinematic differences between them. The combinatorial background companion $L(K/\pi)$ shape is taken to consist of a mixture of pions, protons, and kaons, and its normalisation is left floating in the multivariate fit. The companion $L(K/\pi)$ shape for fully or partially reconstructed backgrounds is obtained by weighting the PID calibration samples to match the event distributions of simulated events, for each background type.

5 Multivariate fit to $\mathbf{B_s^0 \to D_s^\mp K^\pm}$ and $\mathbf{B_s^0 \to D_s^- \pi^+}$

The total PDF for the multivariate fit is built from the product of the signal and background PDFs, since correlations between the fitting variables are measured to be small in simulation. These product PDFs are then added for each D_s^- decay mode, and almost all background yields are left free to float. The only exceptions are those backgrounds whose yield is below 2% of the signal yield. These are $B^0 \to D^- K^+$, $B^0 \to D^- \pi^+$, $\overline{\Lambda}_b^0 \to \overline{\Lambda}_c^- K^+$, and $\overline{\Lambda}_b^0 \to \overline{\Lambda}_c^- \pi^+$ for the $B_s^0 \to D_s^\mp K^\pm$ fit, and $B^0 \to D^- \pi^+$, $\overline{\Lambda}_b^0 \to \overline{\Lambda}_c^- \pi^+$, and $B_s^0 \to D_s^\mp K^\pm$ for the $B_s^0 \to D_s^- \pi^+$ fit. These background yields are fixed from known branching fractions and relative efficiencies measured using simulated events. The multivariate fit results in a signal yield of $28\,260 \pm 180$ $B_s^0 \to D_s^- \pi^+$ and 1770 ± 50 $B_s^0 \to D_s^\mp K^\pm$ decays, with an effective purity of 85% for $B_s^0 \to D_s^- \pi^+$ and 74% for $B_s^0 \to D_s^\mp K^\pm$. The multivariate fit is checked for biases using large samples of data-like pseudoexperiments, and none is found. The results of the multivariate fit are shown in Fig. 3 for both the $B_s^0 \to D_s^- \pi^+$ and $B_s^0 \to D_s^\mp K^\pm$, summed over all D_s^- decay modes.

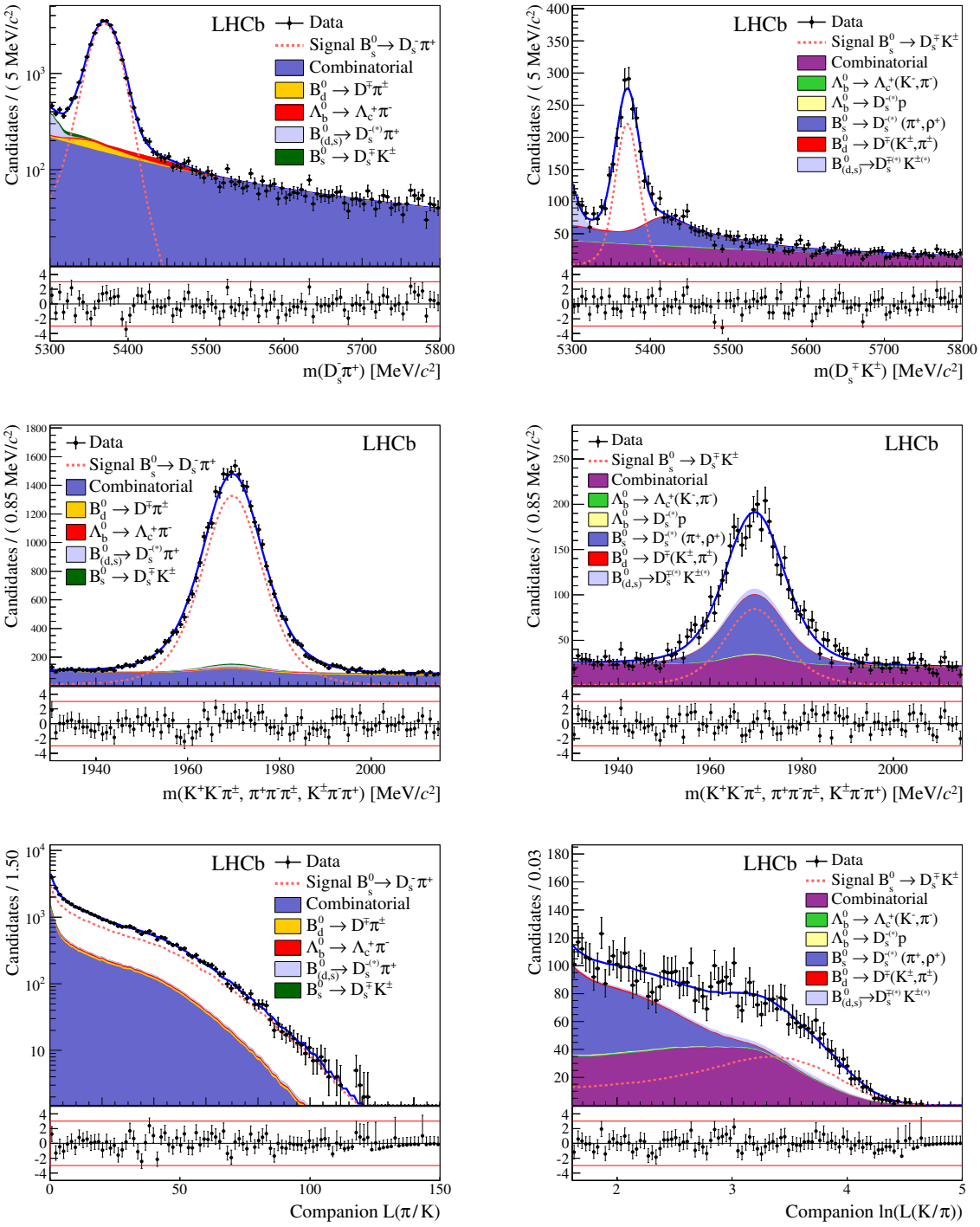

Figure 3: The multivariate fit to the (left) $B_s^0 \to D_s^- \pi^+$ and (right) $B_s^0 \to D_s^\mp K^\pm$ candidates for all D_s^- decay modes combined. From top to bottom: distributions of candidates in B_s^0 mass, D_s^- mass, companion PID log-likelihood difference. The solid, blue, line represents the sum of the fit components.

6 Flavour Tagging

At the LHC, b quarks are produced in pairs $b\bar{b}$; one of the two hadronises to form the signal B_s^0, the other b quark hadronises and decays independently. The identification of the B_s^0 initial flavour is performed by means of two flavour-tagging algorithms which exploit this pair-wise production of b quarks. The opposite side (OS) tagger determines the flavour of the non-signal b-hadron produced in the proton-proton collision using the charge of the lepton (μ, e) produced in semileptonic B decays, or that of the kaon from the $b \to c \to s$ decay chain, or the charge of the inclusive secondary vertex reconstructed from b-decay products. The same side kaon (SSK) tagger searches for an additional charged kaon accompanying the fragmentation of the signal B_s^0 or $\overline{B}_s^0$.

Each of these algorithms has an intrinsic mistag rate ω = (wrong tags)/(all tags) and a tagging efficiency $\varepsilon_{\rm tag}$ = (tagged candidates)/(all candidates). Candidates can be tagged incorrectly due to tracks from the underlying event, particle misidentifications, or flavour oscillations of neutral B mesons. The intrinsic mistag ω can only be measured in flavour-specific, self-tagging final states.

The tagging algorithms predict for each B_s^0 candidate an estimate η of the mistag probability, which should closely follow the intrinsic mistag ω. This estimate η is obtained by using a neural network trained on simulated events whose inputs are the kinematic, geometric, and PID properties of the tagging particle(s).

The estimated mistag η is treated as a per-candidate variable, thus adding an observable to the fit. Due to variations in the properties of tagging tracks for different channels, the predicted mistag probability η is usually not exactly the (true) mistag rate ω, which requires η to be calibrated using flavour specific, and therefore self-tagging, decays. The statistical uncertainty on C_f, S_f, and $S_{\overline{f}}$ scales with $1/\sqrt{\varepsilon_{\rm eff}}$, defined as $\varepsilon_{\rm eff} = \varepsilon_{\rm tag}(1-2\omega)^2$. Therefore, the tagging algorithms are tuned for maximum effective tagging power $\varepsilon_{\rm eff}$.

6.1 Tagging calibration

The calibration for the OS tagger is performed using several control channels: $B^+ \to J/\psi\, K^+$, $B^+ \to \overline{D}^0\pi^+$, $B^0 \to D^{*-}\mu^+\nu_\mu$, $B^0 \to J/\psi\, K^{*0}$ and $B_s^0 \to D_s^-\pi^+$. This calibration of η is done for each control channel using the linear function

$$\omega = p_0 + p_1 \cdot (\eta - \langle\eta\rangle)\,, \tag{7}$$

where the values of p_0 and p_1 are called calibration parameters, and $\langle\eta\rangle$ is the mean of the η distribution predicted by a tagger in a specific control channel. Systematic uncertainties are assigned to account for possible dependences of the calibration parameters on the final state considered, on the kinematics of the B_s^0 candidate and on the event properties. The corresponding values of the calibration parameters are summarised in Table 1. For each control channel the relevant calibration parameters are reported with their statistical and systematic uncertainties. These are averaged to give the reference values including a systematic uncertainty accounting for kinematic differences between different channels. The resulting calibration parameters for the $B_s^0 \to D_s^\mp K^\pm$ fit are: $p_0 = 0.3834 \pm 0.0014 \pm 0.0040$

Table 1: Calibration parameters of the combined OS tagger extracted from different control channels. In each entry the first uncertainty is statistical and the second systematic.

Control channel	$\langle\eta\rangle$	$p_0 - \langle\eta\rangle$	p_1
$B^+ \to J/\psi K^+$	0.3919	$0.0008 \pm 0.0014 \pm 0.0015$	$0.982 \pm 0.017 \pm 0.005$
$B^+ \to \overline{D}^0\pi^+$	0.3836	$0.0018 \pm 0.0016 \pm 0.0015$	$0.972 \pm 0.017 \pm 0.005$
$B^0 \to J/\psi K^{*0}$	0.390	$0.0090 \pm 0.0030 \pm 0.0060$	$0.882 \pm 0.043 \pm 0.039$
$B^0 \to D^{*-}\mu^+\nu_\mu$	0.3872	$0.0081 \pm 0.0019 \pm 0.0069$	$0.946 \pm 0.019 \pm 0.061$
$B_s^0 \to D_s^-\pi^+$	0.3813	$0.0159 \pm 0.0097 \pm 0.0071$	$1.000 \pm 0.116 \pm 0.047$
Average	0.3813	$0.0021 \pm 0.0014 \pm 0.0040$	$0.972 \pm 0.012 \pm 0.035$

and $p_1 = 0.972 \pm 0.012 \pm 0.035$, where the p_0 for each control channel needs to be translated to the $\langle\eta\rangle$ of $B_s^0 \to D_s^-\pi^+$, the channel which is most similar to the signal channel $B_s^0 \to D_s^\mp K^\pm$. This is achieved by the transformation $p_0 \to p_0 + p_1(\langle\eta\rangle - 0.3813)$ in each control channel.

The SSK algorithm uses a neural network to select fragmentation particles, giving improved flavour tagging power [36] with respect to earlier cut-based [37] algorithms. It is calibrated using the $B_s^0 \to D_s^-\pi^+$ channel, resulting in $\langle\eta\rangle = 0.4097$, $p_0 = 0.4244 \pm 0.0086 \pm 0.0071$ and $p_1 = 1.255 \pm 0.140 \pm 0.104$, where the first uncertainty is statistical and second systematic. The systematic uncertainties include the uncertainty on the decay-time resolution, the $B_s^0 \to D_s^-\pi^+$ fit model, and the backgrounds in the $B_s^0 \to D_s^-\pi^+$ fit.

Figure 4 shows the measured mistag probability as a function of the mean predicted mistag probability in $B_s^0 \to D_s^-\pi^+$ decays for the OS and SSK taggers. The data points show a linear correlation corresponding to the functional form in Eq. 7. We additionally validate that the obtained tagging calibration parameters can be used in $B_s^0 \to D_s^\mp K^\pm$ decays by comparing them for $B_s^0 \to D_s^\mp K^\pm$ and $B_s^0 \to D_s^-\pi^+$ in simulated events; we find excellent agreement between the two. We also evaluate possible tagging asymmetries between B and $\overline{B}$ mesons for the OS and SSK taggers by performing the calibrations split by B meson flavour. The OS tagging asymmetries are measured using $B^+ \to J/\psi K^+$ decays, while the SSK tagging asymmetries are measured using prompt $D_s^\pm$ mesons whose $p_{\rm T}$ distribution has been weighted to match the $B_s^0 \to D_s^-\pi^+$ signal. The resulting initial flavour asymmetries for p_0, p_1 and $\varepsilon_{\rm tag}$ are taken into account in the decay-time fit.

6.2 Combination of OS and SSK taggers

Since the SSK and OS taggers rely on different physical processes they are largely independent, with a correlation measured as negligible. The tagged candidates are therefore split into three different samples depending on the tagging decision: events only tagged by the OS tagger (OS-only), those only tagged by the SSK tagger (SSK-only), and those tagged by both the OS and SSK taggers (OS-SSK). For the candidates that have decisions from both taggers a combination is performed using the calibrated mistag probabilities. The combined tagging decision and calibrated mistag rate are used in the final time-dependent fit, where the calibration parameters are constrained using the combination of their as-

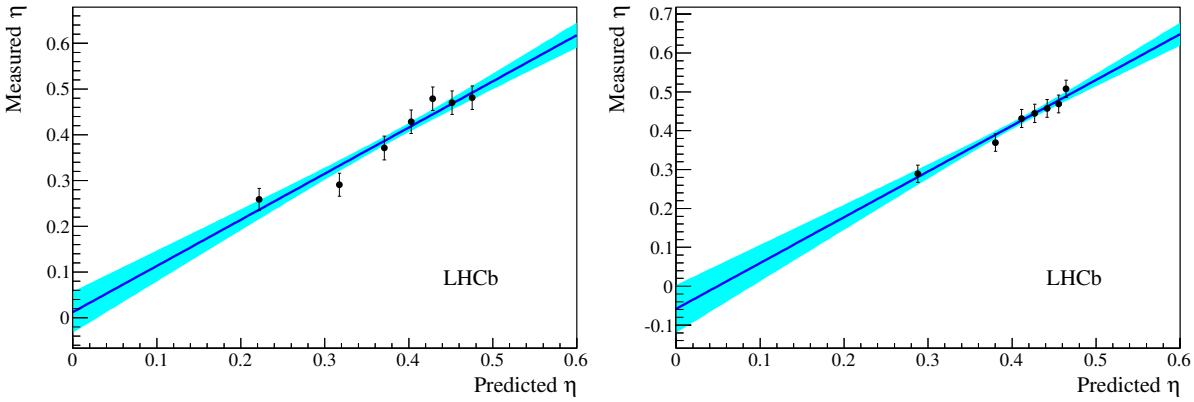

Figure 4: Measured mistag rate against the average predicted mistag rate for the (left) OS and (right) SSK taggers in $B_s^0 \to D_s^- \pi^+$ decays. The error bars represent only the statistical uncertainties. The solid curve is the linear fit to the data points, the shaded area defines the 68% confidence level region of the calibration function (statistical only).

Table 2: Flavour tagging performance for the three different tagging categories for $B_s^0 \to D_s^- \pi^+$ candidates.

Event type	$\varepsilon_{\rm tag}$ [%]	$\varepsilon_{\rm eff}$ [%]
OS-only	19.80 ± 0.23	1.61 ± 0.03 ± 0.08
SSK-only	28.85 ± 0.27	1.31 ± 0.22 ± 0.17
OS-SSK	18.88 ± 0.23	2.15 ± 0.05 ± 0.09
Total	67.53	5.07

sociated statistical and systematic uncertainties. The tagging performances, as well as the effective tagging power, for the three sub-samples and their combination as measured using $B_s^0 \to D_s^- \pi^+$ events are reported in Table 2.

6.3 Mistag distributions

Because the fit uses the per-candidate mistag prediction, it is necessary to model the distribution of this observable for each event category (SS-only, OS-only, OS-SSK for the signal and each background category). The mistag probability distributions for all B_s^0 decay modes, whether signal or background, are obtained using *sWeighted* $B_s^0 \to D_s^- \pi^+$ events. The mistag probability distributions for combinatorial background events are obtained from the upper B_s^0 mass sideband in $B_s^0 \to D_s^- \pi^+$ decays. For B^0 and Λ_b^0 backgrounds the mistag distributions are obtained from *sWeighted* $B^0 \to D^- \pi^+$ events. For the SSK tagger this is justified by the fact that these backgrounds differ by only one spectator quark and should therefore have similar properties with respect to the fragmentation of the $s\overline{s}$ pair. For the OS tagger, the predicted mistag distributions mainly depend on the kinematic properties of the B candidate, which are similar for B^0 and Λ_b^0 backgrounds.

7 Decay-time resolution and acceptance

The decay-time resolution of the detector must be accounted for because of the fast B_s^0–$\overline{B}_s^0$ oscillations. Any mismodelling of the resolution function also potentially biases and affects the precision of the time-dependent *CP* violation observables. The signal decay-time PDF is convolved with a resolution function that has a different width for each candidate, making use of the per-candidate decay-time uncertainty estimated by the decay-time kinematic fit. This approach requires the per-candidate decay-time uncertainty to be calibrated. The calibration is performed using prompt D_s^- mesons combined with a random track and kinematically weighted to give a sample of "fake B_s^0" candidates, which have a true lifetime of zero. From the spread of the observed decay times, a scale factor to the estimated decay time resolution is found to be 1.37 ± 0.10 [38]. Here the uncertainty is dominated by the systematic uncertainty on the similarity between the kinematically weighted "fake B_s^0" candidates and the signal. As with the per-candidate mistag, the distribution of per-candidate decay-time uncertainties is modelled for the signal and each type of background. For the signal these distributions are taken from *sWeighted* data, while for the combinatorial background they are taken from the B_s^0 mass sidebands. For other backgrounds, the decay-time error distributions are obtained from simulated events, which are weighted for the data-simulation differences found in $B_s^0 \to D_s^- \pi^+$ signal events.

In the case of background candidates which are either partially reconstructed or in which a particle is misidentified, the decay-time is incorrectly estimated because either the measured mass of the background candidate, the measured momentum, or both, are systematically misreconstructed. For example, in the case of $B_s^0 \to D_s^- \pi^+$ as a background to $B_s^0 \to D_s^\mp K^\pm$, the momentum measurement is unbiased, while the reconstructed mass is systematically above the true mass, leading to a systematic increase in the reconstructed decay-time. This effect causes an additional non-Gaussian smearing of the decay-time distribution, which is accounted for in the decay time resolution by nonparametric PDFs obtained from simulated events, referred to as k-factor templates.

The decay-time acceptance of $B_s^0 \to D_s^\mp K^\pm$ candidates cannot be floated because its shape is heavily correlated with the *CP* observables. In particular the upper decay-time acceptance is correlated with $A_f^{\Delta\Gamma}$ and $A_{\overline{f}}^{\Delta\Gamma}$. However, in the case of $B_s^0 \to D_s^- \pi^+$, the acceptance can be measured by fixing Γ_s and floating the acceptance parameters. The decay-time acceptance in the $B_s^0 \to D_s^\mp K^\pm$ fit is fixed to that found in the $B_s^0 \to D_s^- \pi^+$ data fit, corrected by the acceptance ratio in the two channels in simulated signal events. These simulated events have been weighted in the manner described in Sec. 4. In all cases, the acceptance is described using segments of smooth polynomial functions ("splines"), which can be implemented in an analytic way in the decay-time fit [39]. The spline boundaries ("knots") were chosen in an ad hoc fashion to model reliably the features of the acceptance shape, and placed at 0.5, 1.0, 1.5, 2.0, 3.0, 12.0 ps. Doubling the number of knots results in negligible changes to the nominal fit result. The decay-time fit to the $B_s^0 \to D_s^- \pi^+$ data is an *sFit* using the signal PDF from Sec. 1.1, with S_f, $S_{\overline{f}}$, $A_f^{\Delta\Gamma}$, and $A_{\overline{f}}^{\Delta\Gamma}$ all fixed to zero, and the knot magnitudes and Δm_s floating. The measured value of $\Delta m_s = 17.772 \pm 0.022\,\mathrm{ps}^{-1}$ (the uncertainty is statistical only) is in excellent agreement

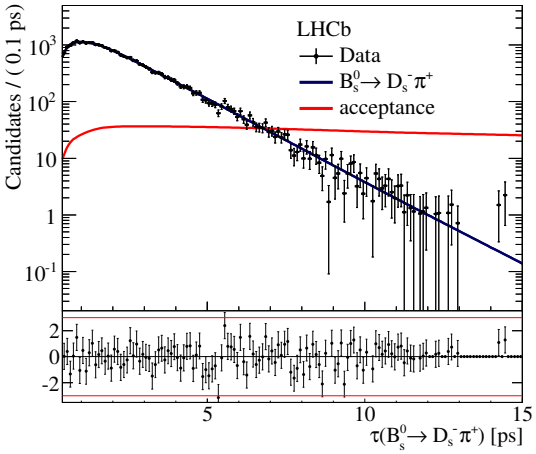

Figure 5: Result of the *sFit* to the decay-time distribution of $B_s^0 \to D_s^- \pi^+$ candidates, which is used to measure the decay-time acceptance in $B_s^0 \to D_s^\mp K^\pm$ decays. The solid curve is measured decay-time acceptance.

with the published LHCb measurement of $\Delta m_s = 17.768 \pm 0.023 \pm 0.006\,\text{ps}^{-1}$ [38]. The time fit to the $B_s^0 \to D_s^- \pi^+$ data together with the measured decay-time acceptance is shown in Fig. 5.

8 Decay-time fit to $\mathbf{B_s^0 \to D_s^\mp K^\pm}$

As described previously, two decay-time fitters are used: in one all signal and background time distributions are described (*cFit*), and in a second the background is statistically subtracted using the *sPlot* technique [15] where only the signal time distributions are described (*sFit*). In both cases an unbinned maximum likelihood fit is performed to the *CP* observables defined in Eq. 5, and the signal decay-time PDF is identical in the two fitters. Both the signal and background PDFs are described in the remainder of this section, but it is important to bear in mind that none of the information about the background PDFs or fixed background parameters is relevant for the *sFit*. When performing the fits to the decay-time distribution, the following parameters are fixed from independent measurements [12, 13, 40]:

$$\Gamma_s = 0.661 \pm 0.007\,\text{ps}^{-1}\,, \quad \Delta\Gamma_s = 0.106 \pm 0.013\,\text{ps}^{-1}\,, \quad \rho(\Gamma_s, \Delta\Gamma_s) = -0.39\,,$$
$$\Gamma_{\Lambda_b^0} = 0.676 \pm 0.006\,\text{ps}^{-1}\,, \quad \Gamma_d = 0.658 \pm 0.003\,\text{ps}^{-1}\,, \quad \Delta m_s = 17.768 \pm 0.024\,\text{ps}^{-1}\,.$$

Here $\rho(\Gamma_s, \Delta\Gamma_s)$ is the correlation between these two measurements, $\Gamma_{\Lambda_b^0}$ is the decay-width of the Λ_b^0 baryon, Γ_d is the B^0 decay width, and Δm_s is the B_s^0 oscillation frequency.

The signal production asymmetry is fixed to zero because the fast B_s^0 oscillations wash out any initial asymmetry and make its effect on the *CP* observables negligible. The signal detection asymmetry is fixed to $(1.0 \pm 0.5)\%$, with the sign convention in which

positive detection asymmetries correspond to a higher efficiency to reconstruct positive kaons [41, 42]. The background production and detection asymmetries are floated within constraints of $\pm 1\%$ for B_s^0 and B^0 decays, and $\pm 3\%$ for Λ_b^0 decays.

The signal and background mistag and decay-time uncertainty distributions, including k-factors, are modelled by kernel templates as described in Sec. 6 and 7. The tagging calibration parameters are constrained to the values obtained from the control channels for all B_s^0 decay modes, except for B^0 and Λ_b^0 decays where the calibration parameters of the SSK tagger are fixed to $p_0 = 0.5$, $p_1 = 0$. All modes use the same spline-based decay-time acceptance function described in Sec. 7.

The backgrounds from B_s^0 decay modes are all flavour-specific, and are modelled by the decay-time PDF used for $B_s^0 \to D_s^- \pi^+$ decays convolved with the appropriate decay-time resolution and k-factors model for the given background. The backgrounds from Λ_b^0 decay modes are all described by a single exponential convolved with the appropriate decay-time resolution and k-factor models. The $B^0 \to D^- K^+$ background is flavour specific and is described with the same PDF as $B_s^0 \to D_s^- \pi^+$, except with Δm_d instead of Δm_s in the oscillating terms, Γ_d instead of Γ_s and the appropriate decay-time resolution and k-factor KEYS templates. The $B^0 \to D^- \pi^+$ background, on the other hand, is not a flavour specific decay, and is itself sensitive to *CP* violation as discussed in Sec. 1. Its decay-time PDF therefore includes nonzero S_f and $S_{\overline{f}}$ terms which are constrained to their world-average values [12]. The decay-time PDF of the combinatorial background used in the *cFit* is a double exponential function split by the tagging category of the event, whose parameters are measured using events in the B_s^0 mass sidebands.

All decay-time PDFs include the effects of flavour tagging, are convolved with a single Gaussian representing the per-candidate decay-time resolution, and are multiplied by the decay-time acceptance described in Sec. 7. Once the decay-time PDFs are constructed, the *sFit* proceeds by fitting the signal PDF to the *sWeighted* $B_s^0 \to D_s^\mp K^\pm$ candidates. The *cFit*, on the other hand, performs a six-dimensional fit to the decay time, decay-time error, predicted mistag, and the three variables used in the multivariate fit. The B_s^0 mass range is restricted to $m(B_s^0) \in [5320, 5420]\,\mathrm{MeV}/c^2$, and the yields of the different signal and background components are fixed to those found in this fit range in the multivariate fit. The decay-time range of the fit is $\tau(B_s^0) \in [0.4, 15.0]\,\mathrm{ps}$ in both cases.

The results of the *cFit* and *sFit* for the *CP* violating observables are given in Table 3, and their correlations in Table 4. The fits to the decay-time distribution are shown in Fig. 6 together with the folded asymmetry plots for $D_s^+ K^-$ and $D_s^- K^+$ final states. The folded asymmetry plots show the difference in the rates of B_s^0 and $\overline{B}_s^0$ tagged $D_s^+ K^-$ and $D_s^- K^+$ candidates, plotted in slices of $2\pi/\Delta m_s$, where the *sWeights* obtained with the multivariate fit have been used to subtract background events. The plotted asymmetry function is drawn using the *sFit* central values of the *CP* observables, and is normalised using the expected dilution due to mistag and time resolution.

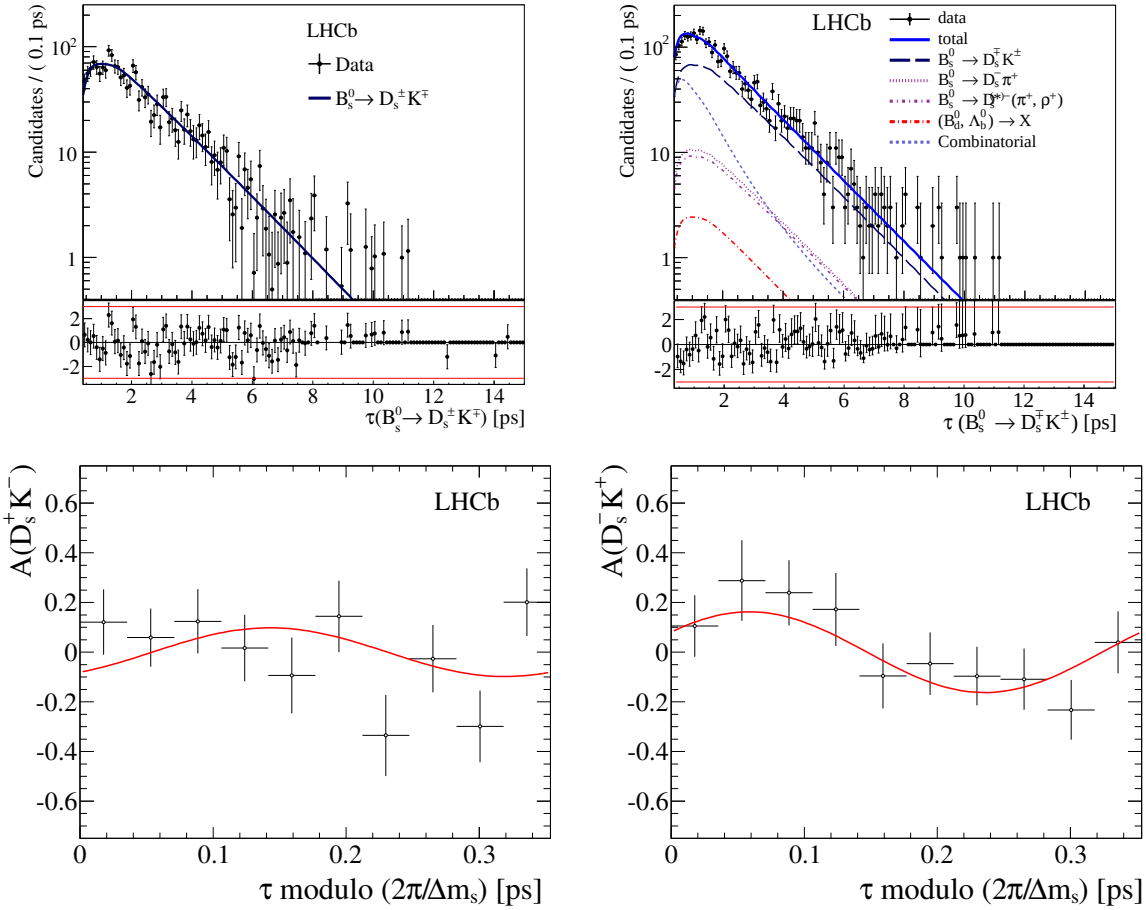

Figure 6: Result of the decay-time (top left) *sFit* and (top right) *cFit* to the $B_s^0 \to D_s^\mp K^\pm$ candidates; the *cFit* plot groups $B_s^0 \to D_s^{*-}\pi^+$ and $B_s^0 \to D_s^- \rho^+$, and also groups $B^0 \to D^- K^+$, $B^0 \to D^-\pi^+$, $\overline{\Lambda}_b^0 \to \overline{\Lambda}_c^- K^+$, $\overline{\Lambda}_b^0 \to \overline{\Lambda}_c^-\pi^+$, $\Lambda_b^0 \to D_s^- p$, $\Lambda_b^0 \to D_s^{*-} p$, and $B^0 \to D_s^- K^+$ together for the sake of clarity. The folded asymmetry plots for (bottom left) $D_s^+ K^-$, and (bottom right) $D_s^- K^+$ are also shown.

Table 3: Fitted values of the *CP* observables to the $B_s^0 \to D_s^\mp K^\pm$ time distribution for (left) *sFit* and (right) *cFit*, where the first uncertainty is statistical, the second is systematic. All parameters other than the *CP* observables are constrained in the fit.

Parameter	*sFit* fitted value	*cFit* fitted value
C_f	$0.52 \pm 0.25 \pm 0.04$	$0.53 \pm 0.25 \pm 0.04$
$A_f^{\Delta\Gamma}$	$0.29 \pm 0.42 \pm 0.17$	$0.37 \pm 0.42 \pm 0.20$
$A_{\overline{f}}^{\Delta\Gamma}$	$0.14 \pm 0.41 \pm 0.18$	$0.20 \pm 0.41 \pm 0.20$
S_f	$-0.90 \pm 0.31 \pm 0.06$	$-1.09 \pm 0.33 \pm 0.08$
$S_{\overline{f}}$	$-0.36 \pm 0.34 \pm 0.06$	$-0.36 \pm 0.34 \pm 0.08$

Table 4: Statistical correlation matrix of the $B_s^0 \to D_s^{\mp} K^{\pm}$ (top) *sFit* and (bottom) *cFit CP* parameters. Other fit parameters have negligible correlations with the *CP* parameters and are omitted for brevity.

Parameter		C_f	$A_f^{\Delta\Gamma}$	$A_{\overline{f}}^{\Delta\Gamma}$	S_f	$S_{\overline{f}}$
sFit	C_f	1.000	0.071	0.097	0.117	−0.042
	$A_f^{\Delta\Gamma}$		1.000	0.500	−0.044	−0.003
	$A_{\overline{f}}^{\Delta\Gamma}$			1.000	−0.013	−0.005
	S_f				1.000	0.007
	$S_{\overline{f}}$					1.000
cFit	C_f	1.000	0.084	0.103	−0.008	−0.045
	$A_f^{\Delta\Gamma}$		1.000	0.544	−0.117	−0.022
	$A_{\overline{f}}^{\Delta\Gamma}$			1.000	−0.067	−0.032
	S_f				1.000	0.002
	$S_{\overline{f}}$					1.000

9 Systematic uncertainties

Systematic uncertainties arise from the fixed parameters Δm_s, Γ_s, and $\Delta\Gamma_s$, and from the limited knowledge of the decay time resolution and acceptance. These uncertainties are estimated using large sets of simulated pseudoexperiments, in which the relevant parameters are varied. The pseudoexperiments are generated with the average of the *cFit* and *sFit* central values reported in Sec. 8. They are subsequently processed by the full data fitting procedure: first the multivariate fit to obtain the *sWeights*, and then the decay time fits. The fitted values of the observables are compared between the nominal fit, where all fixed parameters are kept at their nominal values, and the systematic fit, where each parameter is varied according to its systematic uncertainty. A distribution is formed by normalising the resulting differences to the uncertainties measured in the nominal fit, and the mean and width of this distribution are added in quadrature and conservatively assigned as the systematic uncertainty. The systematic uncertainty on the acceptance is strongly anti-correlated with that due to the fixed value of Γ_s. This is because the acceptance parameters are determined from the fit to $B_s^0 \to D_s^- \pi^+$ data, where Γ_s determines the expected exponential slope, so that the acceptance parameterises any difference between the observed and the expected slope. The systematic pseudoexperiments are also used to compute the systematic covariance matrix due to each source of uncertainty.

The total systematic covariance matrix is obtained by adding the individual covariance matrices. The resulting systematic uncertainties are shown in Tables 5 and 6 relative to the corresponding statistical uncertainties. The contributions from Γ_s and $\Delta\Gamma_s$ are listed independently for comparison to convey a feeling for their relative importance. For this comparison, Γ_s and $\Delta\Gamma_s$ are treated as uncorrelated systematic effects. When computing the total, however, the correlations between these two, as well as between them and the acceptance parameters, are accounted for, and the full systematic uncertainty which enters

into the total is listed as "acceptance, Γ_s, $\Delta\Gamma_s$". The *cFit* contains fixed parameters describing the decay time of the combinatorial background. These parameters are found to be correlated to the *CP* parameters, and a systematic uncertainty is assigned.

The result is cross-checked by splitting the sample into two subsets according to the two magnet polarities, the hardware trigger decision, and the BDTG response. There is

Table 5: Systematic errors, relative to the statistical error, for (top) *sFit* and (bottom) *cFit*. The daggered contributions (Γ_s, $\Delta\Gamma_s$) are given separately for comparison (see text) with the other uncertainties and are not added in quadrature to produce the total.

Parameter		C_f	$A_f^{\Delta\Gamma}$	$A_{\overline{f}}^{\Delta\Gamma}$	S_f	$S_{\overline{f}}$
sFit	Δm_s	0.062	0.013	0.013	0.104	0.100
	scale factor	0.104	0.004	0.004	0.092	0.096
	${\Delta\Gamma_s}^\dagger$	0.007	0.261	0.286	0.007	0.007
	${\Gamma_s}^\dagger$	0.043	0.384	0.385	0.039	0.038
	acceptance, Γ_s, $\Delta\Gamma_s$	0.043	0.427	0.437	0.039	0.038
	sample splits	0.124	0.000	0.000	0.072	0.071
	total	0.179	0.427	0.437	0.161	0.160
cFit	Δm_s	0.068	0.014	0.011	0.131	0.126
	scale factor	0.131	0.004	0.004	0.101	0.103
	${\Delta\Gamma_s}^\dagger$	0.008	0.265	0.274	0.009	0.008
	${\Gamma_s}^\dagger$	0.049	0.395	0.394	0.048	0.042
	acceptance, Γ_s, $\Delta\Gamma_s$	0.050	0.461	0.464	0.050	0.043
	comb. bkg. lifetime	0.016	0.069	0.072	0.015	0.005
	sample splits	0.102	0.000	0.000	0.156	0.151
	total	0.187	0.466	0.470	0.234	0.226

Table 6: Systematic uncertainty correlations for (top) *sFit* and (bottom) *cFit*.

Parameter		C_f	$A_f^{\Delta\Gamma}$	$A_{\overline{f}}^{\Delta\Gamma}$	S_f	$S_{\overline{f}}$
sFit	C_f	1.00	0.18	0.18	−0.04	−0.04
	$A_f^{\Delta\Gamma}$		1.00	0.95	−0.17	−0.16
	$A_{\overline{f}}^{\Delta\Gamma}$			1.00	−0.17	−0.16
	S_f				1.00	0.05
	$S_{\overline{f}}$					1.00
cFit	C_f	1.00	0.22	0.22	−0.04	−0.03
	$A_f^{\Delta\Gamma}$		1.00	0.96	−0.17	−0.14
	$A_{\overline{f}}^{\Delta\Gamma}$			1.00	−0.17	−0.14
	S_f				1.00	0.09
	$S_{\overline{f}}$					1.00

good agreement between the *cFit* and the *sFit* in each subsample. However, when the sample is split by BDTG response, the weighted averages of the subsamples show a small discrepancy with the nominal fit for C_f, S_f, and $S_{\overline{f}}$, and a corresponding systematic uncertainty is assigned. In addition, fully simulated signal and background events are fitted in order to check for systematic effects due to neglecting correlations between the different variables in the signal and background PDFs. No bias is found.

A potential source of systematic uncertainty is the imperfect knowledge on the tagging parameters p_0 and p_1. Their uncertainties are propagated into the nominal fits by means of Gaussian constraints, and are therefore included in the statistical error. A number of other possible systematic effects were studied, but found to be negligible. These include possible production and detection asymmetries, and missing or imperfectly modelled backgrounds. Potential systematic effects due to fixed background yields are evaluated by generating pseudoexperiments with the nominal value for these yields, and fitting back with the yields fixed to twice their nominal value. No significant bias is observed and no systematic uncertainty assigned. No systematic uncertainty is attributed to the imperfect knowledge of the momentum and longitudinal scale of the detector since both effects are taken into account by the systematic uncertainty in Δm_s.

Both the *cFit* and *sFit* are found to be unbiased through studies of large ensembles of pseudoexperiments generated at the best-fit point in data. In addition, differences between the *cFit* and *sFit* are evaluated from the distributions of the per-pseudoexperiment differences of the fitted values. Both fitters return compatible results. Indeed, an important result of this analysis is that the *sFit* technique has been successfully used in an environment with such a large number of variables, parameters and categories. The *sFit* technique was able to perform an accurate subtraction of a variety of time-dependent backgrounds in a multidimensional fit, including different oscillation frequencies, different tagging behaviours, and backgrounds with modified decay-time distributions due to misreconstructed particles.

10 Interpretation

The measurement of the *CP*-sensitive parameters is interpreted in terms of $\gamma - 2\beta_s$ and subsequently γ. For this purpose we have arbitrarily chosen the *cFit* as the nominal fit result. The strategy is to maximise the following likelihood

$$\mathcal{L}(\vec{\alpha}) = \exp\left(-\frac{1}{2}\left(\vec{A}(\vec{\alpha}) - \vec{A}_{\rm obs}\right)^T V^{-1}\left(\vec{A}(\vec{\alpha}) - \vec{A}_{\rm obs}\right)\right), \tag{8}$$

where $\vec{\alpha} = (\gamma, \phi_s, r_{D_sK}, \delta)$ is the vector of the physics parameters, $\vec{A}$ is the vector of observables expressed through Eqs. 6, $\vec{A}_{\rm obs}$ is the vector of the measured *CP* violating observables and V is the experimental (statistical and systematic) covariance matrix. Confidence intervals are computed by evaluating the test statistic $\Delta\chi^2 \equiv \chi^2(\vec{\alpha}'_{\rm min}) - \chi^2(\vec{\alpha}_{\rm min})$, where $\chi^2(\vec{\alpha}) = -2\ln\mathcal{L}(\vec{\alpha})$, in a frequentist way following Ref. [43]. Here, $\vec{\alpha}_{\rm min}$ denotes the global maximum of Eq. 8, and $\vec{\alpha}'_{\rm min}$ is the conditional maximum when the parameter of interest is fixed to the tested value. The value of β_s is constrained to the LHCb measurement from

$B_s^0 \to J/\psi K^+K^-$ and $B_s^0 \to J/\psi \pi^+\pi^-$ decays, $\phi_s = 0.01 \pm 0.07\,(\text{stat}) \pm 0.01\,(\text{syst})$ rad [13]. Neglecting penguin pollution and assuming no BSM contribution in these decays, $\phi_s = -2\beta_s$. The resulting confidence intervals are, at 68% CL,

$$\begin{aligned} \gamma &= (115^{+28}_{-43})^\circ\,, \\ \delta &= (3^{+19}_{-20})^\circ\,, \\ r_{D_sK} &= 0.53^{+0.17}_{-0.16}\,, \end{aligned}$$

where the intervals for the angles are expressed modulo 180°. Figure 7 shows the $1-\text{CL}$ curve for γ, and the two-dimensional contours of the profile likelihood $\mathcal{L}(\vec{\alpha}'_{\text{min}})$. The systematic contributions to the uncertainty are quoted separately as $\gamma = \left(115^{+26}_{-35}\,(\text{stat})^{+8}_{-25}\,(\text{syst}) \pm 4\,(\phi_s)\right)^\circ$, assuming the central value to be independent from

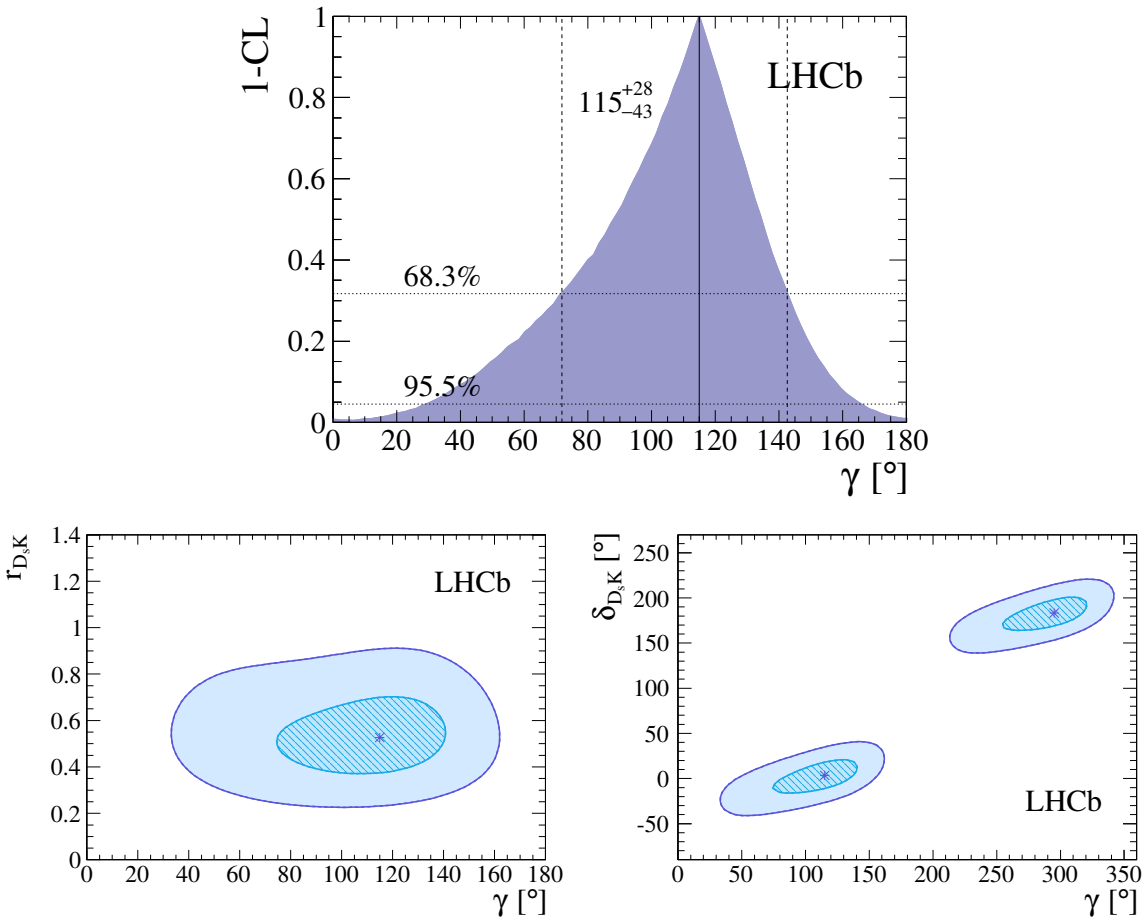

Figure 7: Graph showing $1-\text{CL}$ for γ, together with the central value and the 68.3% CL interval as obtained from the frequentist method described in the text (top). Profile likelihood contours of r_{D_sK} vs. γ (bottom left), and δ vs. γ (bottom right). The contours are the 1σ (2σ) profile likelihood contours, where $\Delta\chi^2 = 1$ ($\Delta\chi^2 = 4$), corresponding to 39% CL (86% CL) in Gaussian approximation. The markers denote the best-fit values.

systematic uncertainties and taking the difference in squares of the total and statistical uncertainties.

11 Conclusion

The *CP* violation sensitive parameters which describe the $B_s^0 \to D_s^{\mp} K^{\pm}$ decay rates have been measured using a dataset of $1.0\,\text{fb}^{-1}$ of pp collision data. Their values are found to be

$$\begin{aligned} C_f &= 0.53 \pm 0.25 \pm 0.04\,, \\ A_f^{\Delta\Gamma} &= 0.37 \pm 0.42 \pm 0.20\,, \\ A_{\overline{f}}^{\Delta\Gamma} &= 0.20 \pm 0.41 \pm 0.20\,, \\ S_f &= -1.09 \pm 0.33 \pm 0.08\,, \\ S_{\overline{f}} &= -0.36 \pm 0.34 \pm 0.08\,, \end{aligned}$$

where the first uncertainties are statistical and the second are systematic. The results are interpreted in terms of the CKM angle γ, which yields $\gamma = (115^{+28}_{-43})^\circ$, $\delta = (3^{+19}_{-20})^\circ$ and $r_{D_sK} = 0.53^{+0.17}_{-0.16}$ (all angles are given modulo 180°) at the 68% confidence level. This is the first measurement of γ performed in this channel.

Acknowledgements

We express our gratitude to our colleagues in the CERN accelerator departments for the excellent performance of the LHC. We thank the technical and administrative staff at the LHCb institutes. We acknowledge support from CERN and from the national agencies: CAPES, CNPq, FAPERJ and FINEP (Brazil); NSFC (China); CNRS/IN2P3 (France); BMBF, DFG, HGF and MPG (Germany); SFI (Ireland); INFN (Italy); FOM and NWO (The Netherlands); MNiSW and NCN (Poland); MEN/IFA (Romania); MinES and FANO (Russia); MinECo (Spain); SNSF and SER (Switzerland); NASU (Ukraine); STFC (United Kingdom); NSF (USA). The Tier1 computing centres are supported by IN2P3 (France), KIT and BMBF (Germany), INFN (Italy), NWO and SURF (The Netherlands), PIC (Spain), GridPP (United Kingdom). We are indebted to the communities behind the multiple open source software packages on which we depend. We are also thankful for the computing resources and the access to software R&D tools provided by Yandex LLC (Russia). Individual groups or members have received support from EPLANET, Marie Skłodowska-Curie Actions and ERC (European Union), Conseil général de Haute-Savoie, Labex ENIGMASS and OCEVU, Région Auvergne (France), RFBR (Russia), XuntaGal and GENCAT (Spain), Royal Society and Royal Commission for the Exhibition of 1851 (United Kingdom).

References

[1] N. Cabibbo, *Unitary symmetry and leptonic decays*, Phys. Rev. Lett. **10** (1963) 531.

[2] M. Kobayashi and T. Maskawa, *CP Violation in the Renormalizable Theory of Weak Interaction*, Prog. Theor. Phys. **49** (1973) 652.

[3] I. Dunietz and R. G. Sachs, *Asymmetry Between Inclusive Charmed and Anticharmed Modes in B^0, Anti-B^0 Decay as a Measure of CP Violation*, Phys. Rev. **D37** (1988) 3186.

[4] R. Aleksan, I. Dunietz, and B. Kayser, *Determining the CP violating phase γ*, Z. Phys. **C54** (1992) 653.

[5] R. Fleischer, *New strategies to obtain insights into CP violation through $B_{(s)} \to D^{\pm}_{(s)} K^{\mp}$, $D^{*\pm}_{(s)} K^{\mp}$, ... and $B_{(d)} \to D^{\pm}\pi^{\mp}$, $D^{*\pm}\pi^{\mp}$, ... decays*, Nucl. Phys. **B671** (2003) 459, arXiv:hep-ph/0304027.

[6] BaBar collaboration, B. Aubert *et al.*, *Measurement of time-dependent CP-violating asymmetries and constraints on* $\sin(2\beta+\gamma)$ *with partial reconstruction of $B \to D^{*\mp}\pi^{\pm}$ decays*, Phys. Rev. **D71** (2005) 112003, arXiv:hep-ex/0504035.

[7] BaBar collaboration, B. Aubert *et al.*, *Measurement of time-dependent CP asymmetries in $B^0 \to D^{(*)\pm}\pi^{\mp}$ and $B^0 \to D^{\pm}\rho^{\mp}$ decays*, Phys. Rev. D **73** (2006) 111101, arXiv:hep-ex/0602049.

[8] Belle collaboration, F. J. Ronga *et al.*, *Measurement of CP violation in $B^0 \to D^{*-}\pi^+$ and $B^0 \to D^-\pi^+$ decays*, Phys. Rev. **D73** (2006) 092003.

[9] Belle collaboration, S. Bahinipati *et al.*, *Measurements of time-dependent CP asymmetries in $B \to D^{*\mp}\pi^{\pm}$ decays using a partial reconstruction technique*, Phys. Rev. **D84** (2011) 021101, arXiv:1102.0888.

[10] M. A. Baak, *Measurement of CKM angle gamma with charmed B^0 meson decays*, PhD thesis, Vrije Universiteit Amsterdam, 2007, SLAC-R-858.

[11] L. Wolfenstein, *Parametrization of the Kobayashi-Maskawa matrix*, Phys. Rev. Lett. **51** (1983) 1945.

[12] Particle Data Group, J. Beringer *et al.*, *Review of Particle Physics*, Phys. Rev. **D86** (2012) 010001.

[13] LHCb collaboration, R. Aaij *et al.*, *Measurement of CP violation and the B^0_s meson decay width difference with $B^0_s \to J/\psi K^+K^-$ and $B^0_s \to J/\psi\pi^+\pi^-$ decays*, Phys. Rev. **D87** (2013) 112010, arXiv:1304.2600.

[14] LHCb collaboration, R. Aaij *et al.*, *Determination of the sign of the decay width difference in the B^0_s system*, Phys. Rev. Lett. **108** (2012) 241801, arXiv:1202.4717.

[15] M. Pivk and F. R. Le Diberder, *sPlot: a statistical tool to unfold data distributions*, Nucl. Instrum. Meth. **A555** (2005) 356, arXiv:physics/0402083.

[16] Y. Xie, *sFit: a method for background subtraction in maximum likelihood fit*, arXiv:0905.0724.

[17] LHCb collaboration, A. A. Alves Jr. *et al.*, *The LHCb detector at the LHC*, JINST **3** (2008) S08005.

[18] R. Aaij *et al.*, *Performance of the LHCb Vertex Locator*, arXiv:1405.7808, submitted to JINST.

[19] R. Arink *et al.*, *Performance of the LHCb Outer Tracker*, JINST **9** (2014) P01002, arXiv:1311.3893.

[20] M. Adinolfi *et al.*, *Performance of the LHCb RICH detector at the LHC*, Eur. Phys. J. **C73** (2013) 2431, arXiv:1211.6759.

[21] R. Aaij *et al.*, *The LHCb trigger and its performance in 2011*, JINST **8** (2013) P04022, arXiv:1211.3055.

[22] V. V. Gligorov and M. Williams, *Efficient, reliable and fast high-level triggering using a bonsai boosted decision tree*, JINST **8** (2013) P02013, arXiv:1210.6861.

[23] T. Sjöstrand, S. Mrenna, and P. Skands, *PYTHIA 6.4 physics and manual*, JHEP **05** (2006) 026, arXiv:hep-ph/0603175.

[24] I. Belyaev *et al.*, *Handling of the generation of primary events in* Gauss*, the LHCb simulation framework*, Nuclear Science Symposium Conference Record (NSS/MIC) **IEEE** (2010) 1155.

[25] D. J. Lange, *The EvtGen particle decay simulation package*, Nucl. Instrum. Meth. **A462** (2001) 152.

[26] P. Golonka and Z. Was, *PHOTOS Monte Carlo: a precision tool for QED corrections in Z and W decays*, Eur. Phys. J. **C45** (2006) 97, arXiv:hep-ph/0506026.

[27] Geant4 collaboration, J. Allison *et al.*, *Geant4 developments and applications*, IEEE Trans. Nucl. Sci. **53** (2006) 270.

[28] Geant4 collaboration, S. Agostinelli *et al.*, *Geant4: a simulation toolkit*, Nucl. Instrum. Meth. **A506** (2003) 250.

[29] M. Clemencic *et al.*, *The LHCb simulation application,* Gauss*: design, evolution and experience*, J. Phys. Conf. Ser. **331** (2011) 032023.

[30] W. D. Hulsbergen, *Decay chain fitting with a Kalman filter*, NIMA **552** (2005), no. 3 566 .

[31] L. Breiman, J. H. Friedman, R. A. Olshen, and C. J. Stone, *Classification and regression trees*, Wadsworth international group, Belmont, California, USA, 1984.

[32] A. Hocker *et al.*, *TMVA - toolkit for multivariate data analysis*, PoS **ACAT** (2007) 040, arXiv:physics/0703039.

[33] A. Powell *et al.*, *Particle identification at LHCb*, PoS **ICHEP2010** (2010) 020, LHCb-PROC-2011-008.

[34] T. Skwarnicki, *A study of the radiative cascade transitions between the Upsilon-prime and Upsilon resonances*, PhD thesis, Institute of Nuclear Physics, Krakow, 1986, DESY-F31-86-02.

[35] K. S. Cranmer, *Kernel estimation in high-energy physics*, Comput. Phys. Commun. **136** (2001) 198, arXiv:hep-ex/0011057.

[36] G. A. Krocker, *Development and calibration of a same side kaon tagging algorithm and measurement of the B_s^0-$\bar{B}_s^0$ oscillation frequency Δm_s at the LHCb experiment*, PhD thesis, Heidelberg U., Sep, 2013, CERN-THESIS-2013-213.

[37] LHCb collaboration, *Optimization and calibration of the same-side kaon tagging algorithm using hadronic B_s^0 decays in 2011 data*, LHCb-CONF-2012-033.

[38] LHCb collaboration, R. Aaij *et al.*, *Precision measurement of the $B_s^0 - \bar{B}_s^0$ oscillation frequency in the decay $B_s^0 \to D_s^+\pi^-$*, New J. Phys. **15** (2013) 053021, arXiv:1304.4741.

[39] M. Karbach, G. Raven, and M. Schiller, *Decay time integrals in neutral meson mixing and their efficient evaluation*, arXiv:1407.0748.

[40] LHCb collaboration, R. Aaij *et al.*, *Precision measurement of the ratio of the Λ_b^0 to $\bar{B}^0$ lifetimes*, Phys. Lett. **B734** (2014) 122, arXiv:1402.6242.

[41] LHCb collaboration, R. Aaij *et al.*, *Measurement of CP asymmetry in $D^0 \to K^-K^+$ and $D^0 \to \pi^-\pi^+$ decays*, JHEP **07** (2014) 041, arXiv:1405.2797.

[42] LHCb collaboration, R. Aaij *et al.*, *Measurement of D^0–$\bar{D}^0$ mixing parameters and search for CP violation using $D^0 \to K^+\pi^-$ decays*, Phys. Rev. Lett. **111** (2013) 251801, arXiv:1309.6534.

[43] LHCb collaboration, R. Aaij *et al.*, *A measurement of the CKM angle γ from a combination of $B^\pm \to Dh^\pm$ analyses*, Phys. Lett. **B726** (2013) 151, arXiv:1305.2050.

LHCb collaboration

R. Aaij[41], B. Adeva[37], M. Adinolfi[46], A. Affolder[52], Z. Ajaltouni[5], S. Akar[6], J. Albrecht[9], F. Alessio[38], M. Alexander[51], S. Ali[41], G. Alkhazov[30], P. Alvarez Cartelle[37], A.A. Alves Jr[25,38], S. Amato[2], S. Amerio[22], Y. Amhis[7], L. An[3], L. Anderlini[17,g], J. Anderson[40], R. Andreassen[57], M. Andreotti[16,f], J.E. Andrews[58], R.B. Appleby[54], O. Aquines Gutierrez[10], F. Archilli[38], A. Artamonov[35], M. Artuso[59], E. Aslanides[6], G. Auriemma[25,n], M. Baalouch[5], S. Bachmann[11], J.J. Back[48], A. Badalov[36], W. Baldini[16], R.J. Barlow[54], C. Barschel[38], S. Barsuk[7], W. Barter[47], V. Batozskaya[28], V. Battista[39], A. Bay[39], L. Beaucourt[4], J. Beddow[51], F. Bedeschi[23], I. Bediaga[1], S. Belogurov[31], K. Belous[35], I. Belyaev[31], E. Ben-Haim[8], G. Bencivenni[18], S. Benson[38], J. Benton[46], A. Berezhnoy[32], R. Bernet[40], M.-O. Bettler[47], M. van Beuzekom[41], A. Bien[11], S. Bifani[45], T. Bird[54], A. Bizzeti[17,i], P.M. Bjørnstad[54], T. Blake[48], F. Blanc[39], J. Blouw[10], S. Blusk[59], V. Bocci[25], A. Bondar[34], N. Bondar[30,38], W. Bonivento[15,38], S. Borghi[54], A. Borgia[59], M. Borsato[7], T.J.V. Bowcock[52], E. Bowen[40], C. Bozzi[16], T. Brambach[9], J. van den Brand[42], J. Bressieux[39], D. Brett[54], M. Britsch[10], T. Britton[59], J. Brodzicka[54], N.H. Brook[46], H. Brown[52], A. Bursche[40], G. Busetto[22,r], J. Buytaert[38], S. Cadeddu[15], R. Calabrese[16,f], M. Calvi[20,k], M. Calvo Gomez[36,p], P. Campana[18,38], D. Campora Perez[38], A. Carbone[14,d], G. Carboni[24,l], R. Cardinale[19,38,j], A. Cardini[15], L. Carson[50], K. Carvalho Akiba[2], G. Casse[52], L. Cassina[20], L. Castillo Garcia[38], M. Cattaneo[38], Ch. Cauet[9], R. Cenci[58], M. Charles[8], Ph. Charpentier[38], M. Chefdeville[4], S. Chen[54], S.-F. Cheung[55], N. Chiapolini[40], M. Chrzaszcz[40,26], K. Ciba[38], X. Cid Vidal[38], G. Ciezarek[53], P.E.L. Clarke[50], M. Clemencic[38], H.V. Cliff[47], J. Closier[38], V. Coco[38], J. Cogan[6], E. Cogneras[5], P. Collins[38], A. Comerma-Montells[11], A. Contu[15], A. Cook[46], M. Coombes[46], S. Coquereau[8], G. Corti[38], M. Corvo[16,f], I. Counts[56], B. Couturier[38], G.A. Cowan[50], D.C. Craik[48], M. Cruz Torres[60], S. Cunliffe[53], R. Currie[50], C. D'Ambrosio[38], J. Dalseno[46], P. David[8], P.N.Y. David[41], A. Davis[57], K. De Bruyn[41], S. De Capua[54], M. De Cian[11], J.M. De Miranda[1], L. De Paula[2], W. De Silva[57], P. De Simone[18], D. Decamp[4], M. Deckenhoff[9], L. Del Buono[8], N. Déléage[4], D. Derkach[55], O. Deschamps[5], F. Dettori[38], A. Di Canto[38], H. Dijkstra[38], S. Donleavy[52], F. Dordei[11], M. Dorigo[39], A. Dosil Suárez[37], D. Dossett[48], A. Dovbnya[43], K. Dreimanis[52], G. Dujany[54], F. Dupertuis[39], P. Durante[38], R. Dzhelyadin[35], A. Dziurda[26], A. Dzyuba[30], S. Easo[49,38], U. Egede[53], V. Egorychev[31], S. Eidelman[34], S. Eisenhardt[50], U. Eitschberger[9], R. Ekelhof[9], L. Eklund[51], I. El Rifai[5], Ch. Elsasser[40], S. Ely[59], S. Esen[11], H.-M. Evans[47], T. Evans[55], A. Falabella[14], C. Färber[11], C. Farinelli[41], N. Farley[45], S. Farry[52], RF Fay[52], D. Ferguson[50], V. Fernandez Albor[37], F. Ferreira Rodrigues[1], M. Ferro-Luzzi[38], S. Filippov[33], M. Fiore[16,f], M. Fiorini[16,f], M. Firlej[27], C. Fitzpatrick[39], T. Fiutowski[27], M. Fontana[10], F. Fontanelli[19,j], R. Forty[38], O. Francisco[2], M. Frank[38], C. Frei[38], M. Frosini[17,38,g], J. Fu[21,38], E. Furfaro[24,l], A. Gallas Torreira[37], D. Galli[14,d], S. Gallorini[22], S. Gambetta[19,j], M. Gandelman[2], P. Gandini[59], Y. Gao[3], J. García Pardiñas[37], J. Garofoli[59], J. Garra Tico[47], L. Garrido[36], C. Gaspar[38], R. Gauld[55], L. Gavardi[9], G. Gavrilov[30], E. Gersabeck[11], M. Gersabeck[54], T. Gershon[48], Ph. Ghez[4], A. Gianelle[22], S. Giani'[39], V. Gibson[47], L. Giubega[29], V.V. Gligorov[38], C. Göbel[60], D. Golubkov[31], A. Golutvin[53,31,38], A. Gomes[1,a], C. Gotti[20], M. Grabalosa Gándara[5], R. Graciani Diaz[36], L.A. Granado Cardoso[38], E. Graugés[36], G. Graziani[17], A. Grecu[29], E. Greening[55], S. Gregson[47], P. Griffith[45], L. Grillo[11], O. Grünberg[62], B. Gui[59], E. Gushchin[33], Yu. Guz[35,38], T. Gys[38], C. Hadjivasiliou[59], G. Haefeli[39], C. Haen[38], S.C. Haines[47], S. Hall[53], B. Hamilton[58], T. Hampson[46], X. Han[11], S. Hansmann-Menzemer[11], N. Harnew[55], S.T. Harnew[46], J. Harrison[54], J. He[38], T. Head[38], V. Heijne[41], K. Hennessy[52], P. Henrard[5],

L. Henry[8], J.A. Hernando Morata[37], E. van Herwijnen[38], M. Heß[62], A. Hicheur[1], D. Hill[55], M. Hoballah[5], C. Hombach[54], W. Hulsbergen[41], P. Hunt[55], N. Hussain[55], D. Hutchcroft[52], D. Hynds[51], M. Idzik[27], P. Ilten[56], R. Jacobsson[38], A. Jaeger[11], J. Jalocha[55], E. Jans[41], P. Jaton[39], A. Jawahery[58], F. Jing[3], M. John[55], D. Johnson[55], C.R. Jones[47], C. Joram[38], B. Jost[38], N. Jurik[59], M. Kaballo[9], S. Kandybei[43], W. Kanso[6], M. Karacson[38], T.M. Karbach[38], S. Karodia[51], M. Kelsey[59], I.R. Kenyon[45], T. Ketel[42], B. Khanji[20], C. Khurewathanakul[39], S. Klaver[54], K. Klimaszewski[28], O. Kochebina[7], M. Kolpin[11], I. Komarov[39], R.F. Koopman[42], P. Koppenburg[41,38], M. Korolev[32], A. Kozlinskiy[41], L. Kravchuk[33], K. Kreplin[11], M. Kreps[48], G. Krocker[11], P. Krokovny[34], F. Kruse[9], W. Kucewicz[26,o], M. Kucharczyk[20,26,38,k], V. Kudryavtsev[34], K. Kurek[28], T. Kvaratskheliya[31], V.N. La Thi[39], D. Lacarrere[38], G. Lafferty[54], A. Lai[15], D. Lambert[50], R.W. Lambert[42], G. Lanfranchi[18], C. Langenbruch[48], B. Langhans[38], T. Latham[48], C. Lazzeroni[45], R. Le Gac[6], J. van Leerdam[41], J.-P. Lees[4], R. Lefèvre[5], A. Leflat[32], J. Lefrançois[7], S. Leo[23], O. Leroy[6], T. Lesiak[26], B. Leverington[11], Y. Li[3], T. Likhomanenko[63], M. Liles[52], R. Lindner[38], C. Linn[38], F. Lionetto[40], B. Liu[15], S. Lohn[38], I. Longstaff[51], J.H. Lopes[2], N. Lopez-March[39], P. Lowdon[40], H. Lu[3], D. Lucchesi[22,r], H. Luo[50], A. Lupato[22], E. Luppi[16,f], O. Lupton[55], F. Machefert[7], I.V. Machikhiliyan[31], F. Maciuc[29], O. Maev[30], S. Malde[55], A. Malinin[63], G. Manca[15,e], G. Mancinelli[6], J. Maratas[5], J.F. Marchand[4], U. Marconi[14], C. Marin Benito[36], P. Marino[23,t], R. Märki[39], J. Marks[11], G. Martellotti[25], A. Martens[8], A. Martín Sánchez[7], M. Martinelli[39], D. Martinez Santos[42], F. Martinez Vidal[64], D. Martins Tostes[2], A. Massafferri[1], R. Matev[38], Z. Mathe[38], C. Matteuzzi[20], A. Mazurov[16,f], M. McCann[53], J. McCarthy[45], A. McNab[54], R. McNulty[12], B. McSkelly[52], B. Meadows[57], F. Meier[9], M. Meissner[11], M. Merk[41], D.A. Milanes[8], M.-N. Minard[4], N. Moggi[14], J. Molina Rodriguez[60], S. Monteil[5], M. Morandin[22], P. Morawski[27], A. Mordà[6], M.J. Morello[23,t], J. Moron[27], A.-B. Morris[50], R. Mountain[59], F. Muheim[50], K. Müller[40], M. Mussini[14], B. Muster[39], P. Naik[46], T. Nakada[39], R. Nandakumar[49], I. Nasteva[2], M. Needham[50], N. Neri[21], S. Neubert[38], N. Neufeld[38], M. Neuner[11], A.D. Nguyen[39], T.D. Nguyen[39], C. Nguyen-Mau[39,q], M. Nicol[7], V. Niess[5], R. Niet[9], N. Nikitin[32], T. Nikodem[11], A. Novoselov[35], D.P. O'Hanlon[48], A. Oblakowska-Mucha[27], V. Obraztsov[35], S. Oggero[41], S. Ogilvy[51], O. Okhrimenko[44], R. Oldeman[15,e], G. Onderwater[65], M. Orlandea[29], J.M. Otalora Goicochea[2], P. Owen[53], A. Oyanguren[64], B.K. Pal[59], A. Palano[13,c], F. Palombo[21,u], M. Palutan[18], J. Panman[38], A. Papanestis[49,38], M. Pappagallo[51], L.L. Pappalardo[16,f], C. Parkes[54], C.J. Parkinson[9,45], G. Passaleva[17], G.D. Patel[52], M. Patel[53], C. Patrignani[19,j], A. Pazos Alvarez[37], A. Pearce[54], A. Pellegrino[41], M. Pepe Altarelli[38], S. Perazzini[14,d], E. Perez Trigo[37], P. Perret[5], M. Perrin-Terrin[6], L. Pescatore[45], E. Pesen[66], K. Petridis[53], A. Petrolini[19,j], E. Picatoste Olloqui[36], B. Pietrzyk[4], T. Pilař[48], D. Pinci[25], A. Pistone[19], S. Playfer[50], M. Plo Casasus[37], F. Polci[8], A. Poluektov[48,34], E. Polycarpo[2], A. Popov[35], D. Popov[10], B. Popovici[29], C. Potterat[2], E. Price[46], J. Prisciandaro[39], A. Pritchard[52], C. Prouve[46], V. Pugatch[44], A. Puig Navarro[39], G. Punzi[23,s], W. Qian[4], B. Rachwal[26], J.H. Rademacker[46], B. Rakotomiaramanana[39], M. Rama[18], M.S. Rangel[2], I. Raniuk[43], N. Rauschmayr[38], G. Raven[42], S. Reichert[54], M.M. Reid[48], A.C. dos Reis[1], S. Ricciardi[49], S. Richards[46], M. Rihl[38], K. Rinnert[52], V. Rives Molina[36], D.A. Roa Romero[5], P. Robbe[7], A.B. Rodrigues[1], E. Rodrigues[54], P. Rodriguez Perez[54], S. Roiser[38], V. Romanovsky[35], A. Romero Vidal[37], M. Rotondo[22], J. Rouvinet[39], T. Ruf[38], F. Ruffini[23], H. Ruiz[36], P. Ruiz Valls[64], J.J. Saborido Silva[37], N. Sagidova[30], P. Sail[51], B. Saitta[15,e], V. Salustino Guimaraes[2], C. Sanchez Mayordomo[64], B. Sanmartin Sedes[37], R. Santacesaria[25], C. Santamarina Rios[37], E. Santovetti[24,l], A. Sarti[18,m], C. Satriano[25,n], A. Satta[24],

D.M. Saunders[46], M. Savrie[16,f], D. Savrina[31,32], M. Schiller[42], H. Schindler[38], M. Schlupp[9], M. Schmelling[10], B. Schmidt[38], O. Schneider[39], A. Schopper[38], M.-H. Schune[7], R. Schwemmer[38], B. Sciascia[18], A. Sciubba[25], M. Seco[37], A. Semennikov[31], I. Sepp[53], N. Serra[40], J. Serrano[6], L. Sestini[22], P. Seyfert[11], M. Shapkin[35], I. Shapoval[16,43,f], Y. Shcheglov[30], T. Shears[52], L. Shekhtman[34], V. Shevchenko[63], A. Shires[9], R. Silva Coutinho[48], G. Simi[22], M. Sirendi[47], N. Skidmore[46], T. Skwarnicki[59], N.A. Smith[52], E. Smith[55,49], E. Smith[53], J. Smith[47], M. Smith[54], H. Snoek[41], M.D. Sokoloff[57], F.J.P. Soler[51], F. Soomro[39], D. Souza[46], B. Souza De Paula[2], B. Spaan[9], A. Sparkes[50], P. Spradlin[51], S. Sridharan[38], F. Stagni[38], M. Stahl[11], S. Stahl[11], O. Steinkamp[40], O. Stenyakin[35], S. Stevenson[55], S. Stoica[29], S. Stone[59], B. Storaci[40], S. Stracka[23,38], M. Straticiuc[29], U. Straumann[40], R. Stroili[22], V.K. Subbiah[38], L. Sun[57], W. Sutcliffe[53], K. Swientek[27], S. Swientek[9], V. Syropoulos[42], M. Szczekowski[28], P. Szczypka[39,38], D. Szilard[2], T. Szumlak[27], S. T'Jampens[4], M. Teklishyn[7], G. Tellarini[16,f], F. Teubert[38], C. Thomas[55], E. Thomas[38], J. van Tilburg[41], V. Tisserand[4], M. Tobin[39], S. Tolk[42], L. Tomassetti[16,f], D. Tonelli[38], S. Topp-Joergensen[55], N. Torr[55], E. Tournefier[4], S. Tourneur[39], M.T. Tran[39], M. Tresch[40], A. Tsaregorodtsev[6], P. Tsopelas[41], N. Tuning[41], M. Ubeda Garcia[38], A. Ukleja[28], A. Ustyuzhanin[63], U. Uwer[11], V. Vagnoni[14], G. Valenti[14], A. Vallier[7], R. Vazquez Gomez[18], P. Vazquez Regueiro[37], C. Vázquez Sierra[37], S. Vecchi[16], J.J. Velthuis[46], M. Veltri[17,h], G. Veneziano[39], M. Vesterinen[11], B. Viaud[7], D. Vieira[2], M. Vieites Diaz[37], X. Vilasis-Cardona[36,p], A. Vollhardt[40], D. Volyanskyy[10], D. Voong[46], A. Vorobyev[30], V. Vorobyev[34], C. Voß[62], H. Voss[10], J.A. de Vries[41], R. Waldi[62], C. Wallace[48], R. Wallace[12], J. Walsh[23], S. Wandernoth[11], J. Wang[59], D.R. Ward[47], N.K. Watson[45], D. Websdale[53], M. Whitehead[48], J. Wicht[38], D. Wiedner[11], G. Wilkinson[55], M.P. Williams[45], M. Williams[56], F.F. Wilson[49], J. Wimberley[58], J. Wishahi[9], W. Wislicki[28], M. Witek[26], G. Wormser[7], S.A. Wotton[47], S. Wright[47], S. Wu[3], K. Wyllie[38], Y. Xie[61], Z. Xing[59], Z. Xu[39], Z. Yang[3], X. Yuan[3], O. Yushchenko[35], M. Zangoli[14], M. Zavertyaev[10,b], L. Zhang[59], W.C. Zhang[12], Y. Zhang[3], A. Zhelezov[11], A. Zhokhov[31], L. Zhong[3], A. Zvyagin[38].

[1] *Centro Brasileiro de Pesquisas Físicas (CBPF), Rio de Janeiro, Brazil*
[2] *Universidade Federal do Rio de Janeiro (UFRJ), Rio de Janeiro, Brazil*
[3] *Center for High Energy Physics, Tsinghua University, Beijing, China*
[4] *LAPP, Université de Savoie, CNRS/IN2P3, Annecy-Le-Vieux, France*
[5] *Clermont Université, Université Blaise Pascal, CNRS/IN2P3, LPC, Clermont-Ferrand, France*
[6] *CPPM, Aix-Marseille Université, CNRS/IN2P3, Marseille, France*
[7] *LAL, Université Paris-Sud, CNRS/IN2P3, Orsay, France*
[8] *LPNHE, Université Pierre et Marie Curie, Université Paris Diderot, CNRS/IN2P3, Paris, France*
[9] *Fakultät Physik, Technische Universität Dortmund, Dortmund, Germany*
[10] *Max-Planck-Institut für Kernphysik (MPIK), Heidelberg, Germany*
[11] *Physikalisches Institut, Ruprecht-Karls-Universität Heidelberg, Heidelberg, Germany*
[12] *School of Physics, University College Dublin, Dublin, Ireland*
[13] *Sezione INFN di Bari, Bari, Italy*
[14] *Sezione INFN di Bologna, Bologna, Italy*
[15] *Sezione INFN di Cagliari, Cagliari, Italy*
[16] *Sezione INFN di Ferrara, Ferrara, Italy*
[17] *Sezione INFN di Firenze, Firenze, Italy*
[18] *Laboratori Nazionali dell'INFN di Frascati, Frascati, Italy*
[19] *Sezione INFN di Genova, Genova, Italy*
[20] *Sezione INFN di Milano Bicocca, Milano, Italy*
[21] *Sezione INFN di Milano, Milano, Italy*
[22] *Sezione INFN di Padova, Padova, Italy*

[23] *Sezione INFN di Pisa, Pisa, Italy*
[24] *Sezione INFN di Roma Tor Vergata, Roma, Italy*
[25] *Sezione INFN di Roma La Sapienza, Roma, Italy*
[26] *Henryk Niewodniczanski Institute of Nuclear Physics Polish Academy of Sciences, Kraków, Poland*
[27] *AGH - University of Science and Technology, Faculty of Physics and Applied Computer Science, Kraków, Poland*
[28] *National Center for Nuclear Research (NCBJ), Warsaw, Poland*
[29] *Horia Hulubei National Institute of Physics and Nuclear Engineering, Bucharest-Magurele, Romania*
[30] *Petersburg Nuclear Physics Institute (PNPI), Gatchina, Russia*
[31] *Institute of Theoretical and Experimental Physics (ITEP), Moscow, Russia*
[32] *Institute of Nuclear Physics, Moscow State University (SINP MSU), Moscow, Russia*
[33] *Institute for Nuclear Research of the Russian Academy of Sciences (INR RAN), Moscow, Russia*
[34] *Budker Institute of Nuclear Physics (SB RAS) and Novosibirsk State University, Novosibirsk, Russia*
[35] *Institute for High Energy Physics (IHEP), Protvino, Russia*
[36] *Universitat de Barcelona, Barcelona, Spain*
[37] *Universidad de Santiago de Compostela, Santiago de Compostela, Spain*
[38] *European Organization for Nuclear Research (CERN), Geneva, Switzerland*
[39] *Ecole Polytechnique Fédérale de Lausanne (EPFL), Lausanne, Switzerland*
[40] *Physik-Institut, Universität Zürich, Zürich, Switzerland*
[41] *Nikhef National Institute for Subatomic Physics, Amsterdam, The Netherlands*
[42] *Nikhef National Institute for Subatomic Physics and VU University Amsterdam, Amsterdam, The Netherlands*
[43] *NSC Kharkiv Institute of Physics and Technology (NSC KIPT), Kharkiv, Ukraine*
[44] *Institute for Nuclear Research of the National Academy of Sciences (KINR), Kyiv, Ukraine*
[45] *University of Birmingham, Birmingham, United Kingdom*
[46] *H.H. Wills Physics Laboratory, University of Bristol, Bristol, United Kingdom*
[47] *Cavendish Laboratory, University of Cambridge, Cambridge, United Kingdom*
[48] *Department of Physics, University of Warwick, Coventry, United Kingdom*
[49] *STFC Rutherford Appleton Laboratory, Didcot, United Kingdom*
[50] *School of Physics and Astronomy, University of Edinburgh, Edinburgh, United Kingdom*
[51] *School of Physics and Astronomy, University of Glasgow, Glasgow, United Kingdom*
[52] *Oliver Lodge Laboratory, University of Liverpool, Liverpool, United Kingdom*
[53] *Imperial College London, London, United Kingdom*
[54] *School of Physics and Astronomy, University of Manchester, Manchester, United Kingdom*
[55] *Department of Physics, University of Oxford, Oxford, United Kingdom*
[56] *Massachusetts Institute of Technology, Cambridge, MA, United States*
[57] *University of Cincinnati, Cincinnati, OH, United States*
[58] *University of Maryland, College Park, MD, United States*
[59] *Syracuse University, Syracuse, NY, United States*
[60] *Pontifícia Universidade Católica do Rio de Janeiro (PUC-Rio), Rio de Janeiro, Brazil, associated to* [2]
[61] *Institute of Particle Physics, Central China Normal University, Wuhan, Hubei, China, associated to* [3]
[62] *Institut für Physik, Universität Rostock, Rostock, Germany, associated to* [11]
[63] *National Research Centre Kurchatov Institute, Moscow, Russia, associated to* [31]
[64] *Instituto de Fisica Corpuscular (IFIC), Universitat de Valencia-CSIC, Valencia, Spain, associated to* [36]
[65] *KVI - University of Groningen, Groningen, The Netherlands, associated to* [41]
[66] *Celal Bayar University, Manisa, Turkey, associated to* [38]

[a] *Universidade Federal do Triângulo Mineiro (UFTM), Uberaba-MG, Brazil*
[b] *P.N. Lebedev Physical Institute, Russian Academy of Science (LPI RAS), Moscow, Russia*
[c] *Università di Bari, Bari, Italy*
[d] *Università di Bologna, Bologna, Italy*
[e] *Università di Cagliari, Cagliari, Italy*

[f] *Università di Ferrara, Ferrara, Italy*
[g] *Università di Firenze, Firenze, Italy*
[h] *Università di Urbino, Urbino, Italy*
[i] *Università di Modena e Reggio Emilia, Modena, Italy*
[j] *Università di Genova, Genova, Italy*
[k] *Università di Milano Bicocca, Milano, Italy*
[l] *Università di Roma Tor Vergata, Roma, Italy*
[m] *Università di Roma La Sapienza, Roma, Italy*
[n] *Università della Basilicata, Potenza, Italy*
[o] *AGH - University of Science and Technology, Faculty of Computer Science, Electronics and Telecommunications, Kraków, Poland*
[p] *LIFAELS, La Salle, Universitat Ramon Llull, Barcelona, Spain*
[q] *Hanoi University of Science, Hanoi, Viet Nam*
[r] *Università di Padova, Padova, Italy*
[s] *Università di Pisa, Pisa, Italy*
[t] *Scuola Normale Superiore, Pisa, Italy*
[u] *Università degli Studi di Milano, Milano, Italy*